NASA CR-54587
GE R66FPD137

EXPERIMENTAL EVALUATION OF OUTER CASE BLOWING OR BLEEDING OF SINGLE STAGE AXIAL FLOW COMPRESSOR PART I - DESIGN OF ROTOR AND BLEEDING AND BLOWING CONFIGURATIONS

by

R. G. GIFFIN and L. H. SMITH, JR.

prepared for

NATIONAL AERONAUTICS AND SPACE ADMINISTRATION

Contract NAS 3 - 7618

ADVANCED TECHNOLOGY AND DEMONSTRATOR PROGRAMS DEPARTMENT

FLIGHT PROPULSION DIVISION

GENERAL ELECTRIC

LYNN, MASSACHUSETTS/CINCINNATI, OHIO

NASA CR-54587
GE R66FPD137

EXPERIMENTAL EVALUATION OF OUTER CASE BLOWING OR BLEEDING OF SINGLE STAGE AXIAL FLOW COMPRESSOR

PART I - DESIGN OF ROTOR AND BLEEDING AND BLOWING CONFIGURATIONS

by

R. G. Giffin and L. H. Smith, Jr.

prepared for

NATIONAL AERONAUTICS AND SPACE ADMINISTRATION

April 20, 1966

CONTRACT NO. NAS 3-7618

Technical Management
NASA Lewis Research Center
Cleveland, Ohio
John E. McAulay, Project Manager
Donald M. Sandercock, Research Adviser

ADVANCED TECHNOLOGY AND DEMONSTRATOR PROGRAMS DEPARTMENT
GENERAL ELECTRIC
CINCINNATI, OHIO 45215

EXPERIMENTAL EVALUATION OF OUTER CASE BLOWING OR BLEEDING OF SINGLE STAGE AXIAL FLOW COMPRESSOR

PART I - DESIGN OF ROTOR AND BLEEDING AND BLOWING CONFIGURATIONS

by

R. G. Giffin and L. H. Smith, Jr.

ABSTRACT

An axial-flow high-aspect-ratio transonic compressor rotor blade row was designed as a research unit for use in an experimental program to study the effect of case bleed and case blowing at the rotor blade tip on compressor performance and operating range. Three casing bleed and three casing blowing configurations were designed with sufficient capacity to enable the injection or extraction of 4% of the compressor design flow.

SUMMARY

An axial-flow high-aspect-ratio transonic compressor rotor blade row was designed as a research unit for use in an experimental program to study the effect of case bleed and case blowing at the rotor blade tip on compressor performance and operating range. The rotor was designed to produce a total pressure ratio of 1.47 at a corrected specific weight flow of 29.65 lb/sec-sq. ft. frontal area with a tip speed of 1120 ft/sec. The value of the tip diffusion factor is 0.45 and the hub-tip radius ratio is 0.5. Radially constant total pressure but radially varying losses were used in construction of the velocity diagrams. The aspect ratio is 4.5; part-span shrouds will be used to insure satisfactory aero-mechanical performance. The compressor was designed to be compatible with the General Electric Lynn Component Test Operation House Compressor Test Stand. The tip diameter of the compressor is 34".

Three casing bleed and three casing blowing configurations were designed with sufficient capacity to enable the injection or extraction of 4% of the compressor design flow. A plain casing configuration was also designed to provide a base for comparison. In addition, design parameters are presented for a boundary layer trip and inlet screening to permit studying the effects of boundary layer thickness and inlet flow distortion.

INTRODUCTION

Boundary layer control has been used successfully as a means of delaying flow breakdown and thereby improving the over-all aerodynamic performance characteristics of several devices. Some notable examples are supersonic inlets (ref. 1), subsonic inlets (ref. 2), cascade tunnels (ref. 3), and laminar-flow wings (ref. 4). It is speculated that similar improvements in compressor aerodynamic performance can be accomplished by means of boundary layer control in the rotor tip region.

Several experimenters have investigated the three-dimensional flow phenomena that occur in the rotor tip region of axial-flow compressors (refs. 5 and 6) and the similar end-wall flow phenomena in cascades (refs. 7 and 8). The complex nature of these flows is traceable to the interactions of the blade and casing boundary layers, tip clearance, and pressure fields. As a result, the end-region fluid is prone to separation and, for moderate aerodynamic loadings, to complete breakdown.

The fact that this breakdown of the flow at the casing is responsible for compressor stage stall has been appreciated for some time (ref. 5). It is supported by the knowledge that (1) larger aerodynamic loadings are obtained in cascade tests without stall for the rotor-tip-section geometries than are obtained in actual rotors, (2) blade sections which operate well at other radial locations produce a wide variation in loss conditions when placed near the tip, and (3) high-aspect-ratio blade rows stall more easily than lower aspect ratio blade rows made up of geometrically similar blade elements. These all suggest that blade end effects play an important role in stage performance. Stalls can, of course, originate at the hub, although this is uncommon in the first or second stage of a multi-stage compressor.

High-aspect-ratio compressor stages have been found to exhibit less weight flow range than similar stages with lower aspect ratio blading (refs. 9 and 10). Reduced flow range in turn results in poorer off-design performance and lower tolerance levels to inlet flow distortions when such stages are used in a multistage machine. Inasmuch as high-aspect-ratio blading is desirable for compact, lightweight compressors, methods of improving the flow range for such stages must be investigated.

One method under study is use of outer case boundary layer control devices. Accordingly, a high-aspect-ratio transonic blade row will be operated in conjunction with three blowing, three bleed, and plain case configurations. Selected configurations will be tested with increased boundary layer thickness and inlet flow distortion.

This report presents the design of the rotor, blowing and bleed configurations, and associated hardware necessary to perform these tests.

SYMBOLS

The following symbols are used in this report:

C_p	static-pressure-rise coefficient
c_p	specific heat at constant pressure, 0.2399 Btu/lb-°R
D	diffusion factor
e	base of natural system of logarithm
f	frequency, cps
g	acceleration due to gravity, 32.174 ft/sec^2
i	incidence angle, $i = \beta' - \kappa_1$, deg
i_s	incidence angle, $i_s = \beta' - \kappa_s$, deg
J	mechanical equivalent of heat, 778.161 ft-lb/Btu
K_{bk}	effective-area coefficient
M	Mach number
m	factor in deviation angle relation
N	rotational speed, rpm
P	total or stagnation pressure, psia
p	static or stream pressure, psia
R	gas constant, 53.342 ft-lb/lb-°R
r	radius, inches
$\bar{r}$	mean radius, $\bar{r} = (r_{1.0} + r_{1.5})/2$, inches
S	entropy, Btu/lb-°R
T	total or stagnation temperature, °R
t	static or stream temperature, °R
U	rotor speed, ft/sec
V	air velocity, ft/sec
W	weight flow, lb/sec
X	empirical deviation angle adjustment, deg
z	coordinate along axis, inches
β	air angle, TAN $\beta = V_\theta/V_z$, deg
γ	ratio of specific heats
γ°	blade-chord angle, angle on cylindrical surface between blade chord and axial direction, deg

$\delta°$	deviation angle, $\delta° = \beta'-\kappa_2$, deg
ϵ	angle between tangent to streamline projected on meridional plane and axial direction, deg
η	efficiency
$\vec{\iota}_\kappa$	unit vector in direction of intersection of axisymmetric stream surface and blade mean surface, deg
$\vec{\iota}_{\kappa S}$	unit vector in direction of intersection of axisymmetric stream surface and blade suction surface at the leading edge, deg
κ	angle between cylindrical projection of $\vec{\iota}_\kappa$ and axial direction, deg
κ_S	angle between cylindrical projection of $\vec{\iota}_{\kappa S}$ and axial direction, deg
ρ	static or stream density, $lb\text{-}sec^2/ft^4$
σ	solidity, ratio of chord to spacing
φ	blade-camber angle, difference between angles on cylindrical surface of tangents to mean camber line at leading and trailing edges, deg
$\bar{\omega}$	total-pressure-loss coefficient (defined in ref. 12)

Subscripts:

ad	adiabatic
e	equivalent two-dimensional cascade
h	hub
i	arbitrary axial station
i-1	preceding arbitrary axial station
j	air jet for blowing configurations
m	meridional direction
r	radial direction
t	tip
z	axial direction
θ	tangential direction
1	leading edge
1.0	station at inlet to blade row
1.5	station at exit of blade row
2	trailing edge

Superscript:

'	relative to rotor

ROTOR DESIGN

Overall Design Features

A high-aspect-ratio transonic rotor was designed as an instrument for evaluating the effects on performance and operating range of casing bleed and casing blowing. The overall characteristics of the rotor design are contained in the following list.

1. Rotor tip speed, 1120 ft/sec.
2. Inlet hub-tip radius ratio, 0.50.
3. Total-pressure ratio, 1.47, radially constant.
4. Corrected weight flow per unit frontal area, 29.65 lb/sec-sq. ft.
5. Rotor tip solidity, 1.0, with chord radially constant.
6. Rotor tip relative Mach number, 1.2.
7. Rotor tip diffusion factor, 0.45.
8. Rotor blade section, double-circular-arc.
9. Rotor blade aspect ratio, 4.5.
10. Number of rotor blades, 60.
11. Rotor tip diameter, 34 in.

The rotor tip diffusion factor of 0.45 is somewhat higher than is common practice for stages with a radius ratio of 0.5. This moderately large value was selected with the expectation that the boundary layer control devices to be investigated will permit operation at loading levels that exceed those given by conventional design criteria. The remaining items were selected as being typical of a compressor front stage, the most likely application of a boundary layer control device. The rotor tip diameter was selected to be compatible with the General Electric Lynn Component Test Operation House Compressor Test Stand. The overall flowpath is shown in figure 1.

Method of Calculation for Rotor Design

The overall calculation procedure used for this design is outlined in reference 11, and the principal equations used are contained herein in the appendix.

The overall calculation scheme may be summarized as follows: The flow is considered at a number of axial stations (z = constant planes), and the radial-equilibrium equation, energy equation, and continuity condition are employed at each of them to determine the distribution of flow properties from hub to casing. It is necessary, however, that these distributions obtained separately at each station be consistent from station to station and that the radial acceleration which a fluid particle undergoes as it passes from station to station be accounted for in the radial-equilibrium equation. This is done by assuming shapes for the meridional streamlines consistent with the continuity condition at each station and by expressing the radial acceleration in terms of the streamline slope and curvature. A method of solution by iteration is programmed for the General Electric computer under the name Compressor Axisymmetric Flow Determination program, hereafter referred to as CAFD. This program was used for the present design.

A total of twelve calculation stations and ten equal-flow streamtubes were used to arrive at the design vector diagrams for the rotor. Figure 2 shows the locations of the calculation stations and the resulting design streamlines in the neighborhood of the rotor. The first calculation station, 0.2, was located approximately 10" forward of the rotor and the last calculation station, 3.0, was located approximately 15" aft of the rotor (the annulus height at rotor leading edge is 8.5"); the streamline slope and curvature boundary conditions were established at these end stations. Two of the calculation stations were located immediately upstream and downstream of the blade axial projection extremities (stations 1.0 and 1.5, respectively); the vector diagrams at these stations were used for setting the blades. One station internal to the rotor, (station 1.25), located approximately at the blade stacking axis, was included to improve the overall accuracy of the solution by including the effects of blade thickness blockage on the slopes and curvatures at the blade inlet and discharge stations.

Effective-Area Coefficient

In the application of the CAFD procedure to the present design, no attempt was made to calculate the localized velocity variations that occur deep in the annulus wall boundary layers. Instead, the calculated free-stream flow distributions were continued to the annulus boundaries. The weight flow used at each station was related to the actual weight flow by an effective-area coefficient, K_{bk}, that accounts for the displacement thicknesses of the wall boundary layers. Suitable values for the effective-area coefficient

were selected on the basis of past experience; an effective-area coefficient of 0.98 was used at all stations forward of the rotor and 0.95 at all stations aft of the rotor. Since both bleed and blowing boundary layer control schemes will be investigated with this rotor, it was judged unwise to try to account for either bleed or blowing flow rates in the selection of these values.

At calculation stations where physical obstructions to the flow exist, such as stations internal to a blade row, a modifier must be included in the effective-area coefficient to reflect the reduction of flow area. This modifier is, in general, a function of radius since both the circumference and the tangential thickness of the blades are dependent upon radius. The presence of a part-span shroud in the present design was reflected at the internal blade calculation station by distributing the resulting flow area reduction uniformly across the annulus; this method was judged most appropriate within the overall framework of the calculation procedure. The blade thickness blockage was distributed radially as it actually occurred, however. The combined effects of boundary layer, blade thickness, and part-span shroud blockage resulted in effective-area coefficients for the internal blade calculation station varying from 0.895 at the tip to 0.785 at the hub.

Annulus Shape and Axial Velocities

For given overall design requirements, usually specified by weight flow, pressure ratio, and blade speed, the annulus area is the primary factor in determining the level of axial velocity. When selecting axial velocity levels the following factors must be considered: (1) for a given value of blade loading parameter, such as diffusion factor, a reduction in axial velocity across the rotor tends to reduce the pressure ratio capability of the rotor, (2) a large increase in axial velocity tends to choke the annulus or to pose diffusion problems for succeeding blade rows, and (3) the slopes and curvatures of the casing and hub surfaces can sometimes be used effectively to yield axial velocity profiles that tend to strengthen the traditionally weak blade-end regions. An additional factor for consideration in this design is that the rotor is not immediately followed by a stator. Under this circumstance, annulus choke downstream of the rotor becomes an important consideration.

The hub and tip contours for this stage were calculated based on the above considerations and the resulting flow path is shown in figure 1. Figure 2 is an enlargement of the flow path in the neighborhood of the rotor. Included in this figure, for reference purposes, are the streamlines obtained from the design calculations. The rotor inlet and exit axial velocity distributions are plotted in figure 3.

Total-Pressure Ratio and Loss Coefficients

The selection of diffusion factor, solidity, inlet relative velocity and, from the preceeding section, axial velocity ratio for the rotor tip section, permits calculation of the change in angular momentum across this section of the rotor. The change in angular momentum and a suitable rotor total-pressure-loss coefficient determine the rotor total-pressure ratio, 1.47 for this design. The total-pressure ratio was maintained constant over the radial height of the blade. The equations used for these calculations are given in reference 12, except the following definition of diffusion factor was used:

$$D = 1 - \frac{V'_{1.5}}{V'_{1.0}} + \frac{r_{1.5}V_{\theta 1.5} - r_{1.0}V_{\theta 1.0}}{2\,\bar{r}\,\sigma\, V'_{1.0}}$$

This form is preferred when there is a change in radius as the flow passes through a blade row.

The profile loss portions of the rotor total-pressure-loss coefficients used in the CAFD calculations were determined from the NASA method given in reference 12, except that the special curve for the 10% immersion was not used. Additive shock losses were included where the relative inlet Mach number exceeded unity. These losses were calculated by the NASA method given in reference 13. The diffusion factors and Mach numbers used to calculate the total-pressure-loss coefficients were taken from a preliminary rotor design and were therefore slightly different from those calculated in the final design. Figure 4 shows the radial distribution of rotor total-pressure-loss coefficient that was employed.

The radial distributions of adiabatic efficiency and diffusion factor resulting from these assumptions are shown in figures 5 and 6, respectively. In addition, the radial distributions of relative Mach number and relative air angle at rotor inlet and rotor exit and the static-pressure-rise coefficient distribution are shown in figures 7 through 9, respectively.

Rotor Blade Shape Design

A constant-chord 4.5 aspect-ratio rotor employing double-circular-arc blade sections was selected to fulfill the requirements of this design. The design of the rotor sections was performed along streamlines utilizing the projection of reference 14. Briefly, this projection cuts the blades along the axisymmetric surfaces of the meridional flow but views the cross sections by looking along a radial line. Incidence and deviation angles are defined accordingly. Angles in this projection are termed "cascade angles".

The blade design was based on the vector diagrams at station 1.0 for rotor inlet and at station 1.5 for rotor exit; see figure 2. Except at the hub, the axial projections of the rotor leading and trailing edges are somewhat removed from the axial locations of these calculation stations. Reduction of the aerodynamic test data will incorporate a method for correcting quantities from the measurement planes to the blade edges at both inlet and exit. To enable comparison with test results, the design calculations were cross-plotted and extrapolated to determine the edge values of several pertinent parameters. The dashed lines in figures 3, 7, 8, 10 and 11 show the differences between the edge values and the calculation station values for these parameters.

The incidence angles employed in this design are shown in figure 10. These values were selected on the basis of past experience but subject to the additional criterion that the blade throat is adequate so as to preclude the condition of choking. The final rotor geometry was checked for this condition; the effects of radius change and streamtube convergence along streamlines were included and, on the average, the throat area was 8% larger than the capture area. For the transonic Mach numbers at which this rotor must operate, this throat area was judged to be acceptable.

The deviation angles were obtained by applying Carter's Rule (ref. 15) to an equivalent two-dimensional cascade along with an empirical adjustment resulting from experience in the aerodynamic design and performance synthesis of this general type of rotor. The equivalent two-dimensional cascade is defined as having (1) the same inlet conditions, circulation, and incidence as the cascade it is equivalent of, and (2) no change in radius or axial velocity across it. The exit air angle of this equivalent cascade is given by

$$\mathrm{TAN}\beta'_{1.5e} = \frac{r_{1.5}}{r_{1.0}} \times \frac{V_{z1.5}}{V_{z1.0}} \times \mathrm{TAN}\beta'_{1.5} + \frac{U_{1.0}}{V_{z1.0}} \left[1 - \left(\frac{r_{1.5}}{r_{1.0}} \right)^2 \right]$$

The deviation angle was obtained from Carter's Rule using the camber of the equivalent cascade but the stagger of the actual cascade, plus an empirical adjustment, X.

$$\delta^\circ_{1.5} = \frac{\left[\beta'_{1.0} - i_{1.0} - \beta'_{1.5e} + X \right]}{\left[\frac{\sqrt{\sigma}}{m} - 1 \right]} + X$$

The values used for m were those given in reference 15 for circular-arc camber lines. Figure 11 shows the empirical adjustment and the resulting deviation angles for this design.

The double-circular-arc blade sections were specified on cylindrical surfaces. The cylindrical-section leading- and trailing-edge angles were obtained by applying the descriptive geometry effects of meridional angle and blade lean angle to the cascade edge angles. Figure 12 gives plots of the resulting cylindrical-section camber and chord angle distributions. Because the error involved is negligible, the developed cylindrical sections will be interpreted as plane sections normal to the stacking axis for ease of manufacture.

Rotor Blade Aeromechanical Design

The primary considerations for defining an aeromechanically workable configuration consistent with the overall objectives of this program were (1) avoiding self-excited vibration, (2) the response to per-rev excitations, and (3) steady stress conditions.

Because of the moderately high aspect-ratio selected for the design and the uncertainty of the aerodynamic environment associated with the casing bleed and blowing and inlet distortions, part-span shrouds were considered mandatory. Accordingly, the margin over two per-rev excitation was not a problem. Rather, attention was directed toward avoiding resonance of the first flexural frequency with integral-order per-rev excitation at three-per-rev and higher.

The resulting estimated blade vibrational frequencies and anticipated resonance conditions are shown in figure 13.

The estimated incidence angle margin between self-excitation and clean inlet stall is 3° in the tip region at 80% speed, where the incidence margin appears to be smallest. However, the significance of this margin is clouded by the uncertainties of the aerodynamic environment in the tip region associated with the casing bleed and blowing configurations, inlet distortions and manufacturing deviations.

Table 1 is a listing of the pertinent calculated aeromechanical quantities for this design.

TEST VEHICLE

Inlet Ducting

The conditions of zero inlet swirl and moderately thin casing boundary layer require incorporation of a flow straightener in the vehicle inlet and provision for a large area contraction into the test vehicle; see figure 1. The flow straightener has honeycomb type cells which are approximately equivalent to a 7/8" diameter; the length of the cells is 8". An axisymmetric flux plot of the inlet contraction region yields the casing velocity distribution shown in figure 14; the presence of the four struts was ignored for purposes of this calculation. The lack of adverse gradients suggests conditions conducive for a healthy boundary layer.

Outlet Guide Vanes

A set of outlet guide vanes was designed for the vehicle in order to remove swirl and decrease Mach number so that the facility exhaust system pressure drop will be minimized. Since the limiting facility condition occurs during high-flow operation of the rotor, the outlet guide vanes were designed for operation in the high-flow-low-pressure region of the characteristic. This design was accomplished by making an off-design CAFD calculation in which the design relative flow angles were specified at rotor exit, the weight flow increased by 8%, and the rotor efficiency decreased from approximately 90.5% at design to 72%. The resulting average pressure ratio from the rotor is 1.22, which approximates the facility limit for this level of flow. Since the outlet guide vanes have adjustable stagger, any problems associated with their high incidence operation on the high-pressure part of the characteristic can be readily eliminated.

A modified NACA 65-series thickness distribution was selected for the outlet guide vanes and a circular-arc camber line was used. The hub solidity was selected as 1.4, and the chord was maintained constant radially. The aspect ratio is approximately 2.

Distortion Screens

Radial and circumferential distortion screens were designed to provide a total pressure loss of 15% at the rotor inlet instrumentation station. The circumferential screen will cover a 90° arc of the inlet annulus while the radial screen will cover the outer 40% of the inlet annulus. The solidity of the screens for both types of distortion was determined to be 0.54. This value of solidity was arrived at utilizing test data of reference 16 which approximates the desired design, and a correlation of screen total pressure loss coefficient with screen solidity and screen inlet Mach number (ref. 17).

A screen with approximately 0.016 inch wire diameter and 20 mesh will provide the required 0.54 solidity. These distortion screens will be supported by a screen covering the entire annulus whose wire diameter is about 0.092 inches and which has a 3/4 inch mesh.

Boundary Layer Trip

A boundary layer trip was designed to provide a means of determining the effect of an increased boundary layer on performance of the best blowing and the best bleeding configurations. The estimated boundary layer momentum thickness for the plain case is 0.08 inches. Using classical flat-plate turbulent boundary layer theory and test data where a boundary layer trip was utilized, it was determined that an annulus ring which protrudes 0.3 inches into the airstream from the outer casing would approximately double the boundary layer momentum thickness.

CASING BLEED AND BLOWING CONFIGURATIONS

It has been observed experimentally that the tip portion of the first rotor in a compressor is more prone to stall than the balance of the blade (ref. 5). Experience with blade element performance in this region indicates that the static-pressure-rise coefficient, defined as the ratio of static pressure rise to inlet relative dynamic head, is limited to values of 0.45 to 0.50 when stall is approached. If static-pressure-rise coefficients in excess of these values are attempted the result is increased losses and hence low efficiency, with no appreciable increase in pressure rise.

The examination of cascade data, obtained under the condition of two-dimensionality, shows that static-pressure-rise coefficients of about 0.6 can be obtained without losses becoming excessive. Hence it would be expected that a compressor operating without the detrimental effects of wall boundary layers and clearances would not approach stall until the static-pressure-rise coefficient is increased to about 0.6. Under this hypothesis, the augmentation device employed to locally improve the tip element performance need only be sufficient to provide 0.10 to 0.15 units of static-pressure-rise coefficient. Any additional capability could not be used since some other portion of the rotor would be likely to precipitate stall.

Preliminary Analysis of Blowing Configurations

The simplest way in which we can obtain some numerical estimate of the beneficial action of a jet sheet ejected from the casing upstream of the rotor is to consider that the limiting tip element static-pressure-rise coefficient remains at, say, 0.45, but that the inlet relative dynamic pressure to be used with this coefficient is that of the jet. Then, in order to attain the static pressure rise that the free-stream is capable

of (say 60% of the free-stream relative dynamic pressure) it would be necessary for the jet to have a relative dynamic pressure $(0.60)/(0.45) = 1.33$ times that of the free-stream. This is an optimistic answer because it is based upon the implicit assumption that the tip element will be fully bathed in jet flow, whereas actually the amount of jet fluid that can be used does not permit this. On the other hand, it should be possible to design the jet nozzle so that the rotor incidence angle for the jet fluid has a value that is more favorable than normally occurs in a casing boundary layer, so to this extent the answer is pessimistic.

There will be considerable mixing of the jet fluid and the mainstream fluid as it proceeds through the blade row, and this will provide the mechanism for some pressure rise augmentation, as in an ejector or jet pump. Thus an examination of ejector data was undertaken in order to estimate the potential effects of such a mixing process. It is not proposed that the ejector analogy represents the principal mechanism through which blowing will be beneficial, but it was felt that knowledge of the potential magnitude of the phenomenon would be helpful in selecting configurations and analyzing results.

Two observations relative to ejector data are: (1) a substantial mixing length (approximately 10 diameters) is required in order to obtain the full static pressure rise benefit from the momentum interchange between the primary and secondary flows and (2) the mixing length, for a given pressure rise, is greatly reduced by the use of a multiple-jet arrangement. For any increase in static pressure rise obtainable from the augmentation device to be effective in a rotor it must occur, in axial length, before the rotor trailing edge is passed. This length, compared to an equivalent diameter of any reasonable hypothetical ejector model of the tip region, is very short; the ratio of length to equivalent-diameter has an order of magnitude of unity. Examination of the data in references 18 and 19 indicates that the increase in static-pressure-rise coefficient due to the ejector effect will amount to less than 0.05 units for a length-to-diameter ratio of unity.

The data in reference 18 also indicates that a multiple-jet primary ejector will produce nearly twice the increase in static pressure as a single-jet primary ejector for a given short length. Although the expected increase in static-pressure-rise coefficient is small in an absolute sense, it is a significant percentage of the required increase.

To prevent local stalling of the tip section due to poor incidence angle in the region occupied by the jet, the absolute angle at which the jet issues from the casing must be controlled as a function of the absolute jet velocity so as to approximately align the relative flow angle of the jet with the relative flow angle of the free-stream. For purposes of performing calculations, a corrected compressor speed of 70% of design speed was selected, since this is representative of the condition where the augmentation device would be of most benefit for the first stage of a multi-stage compressor. Figure 15 is a velocity diagram showing the relationship between jet velocity and jet flow angle when the rotor is operating near its estimated 70% speed stall point.

Preliminary Analysis of Bleed Configurations

Reference 6 presents detailed measurements that describe the flow field behind the tip region of a rotor. These results show, near the wall, that the axial velocity is small but that the tangential velocity is large. Confirming data are shown in figure 16, which is a photograph of the casing windows from the General Electric four-stage Low Speed Research Compressor. These windows had been in place over the four rotor blade rows when the lamp black and oil flow traces shown were made. In this figure the rotor moves from left to right and the through-flow is downward. There are two crayon lines on each window that indicate the leading-edge and trailing-edge planes of the rotor blades. Also, at certain places crayon marks indicate the locations of adjacent stator vanes. It can be seen that the flow direction in the rotor tip region is primarily circumferential, but near the leading edge there is a through-flow component, while in the rear portion the flow frequently has an upstream component. These flows tend to coalesce at a location in the front half of each blade row. The pattern shown occurred when the compressor was near stall; with more open throttle positions the line of coalescence was further aft. This indicates that the extent of axial back-flow increases in the casing boundary layer as a machine is throttled toward stall. Casing measurements taken upstream and downstream of the third rotor confirm this, and indicate that the displacement thickness of the axial-velocity casing boundary layer increases rapidly as stall is approached. It is reasonable to expect that if this casing boundary layer fluid could be removed, a higher pressure rise could be sustained before stall occurs.

One method of removing the boundary layer is by bleeding through an annular slot. Experiments on diffusers and inlets that incorporate such devices show that their location is important relative to obtaining optimum performance, and as a general rule they are most effective when located near the position at which separation would otherwise occur. This suggests a slot location near the mid-chord position of the rotor or between mid-chord and the leading edge. A slot at this location, however, would locally increase the rotor tip clearance, which is known to have an adverse effect on rotor performance. Thus, large bleed flow rates would be required since the adverse effect of the increased tip clearance would have to be overcome before any net gain could be realized. A casing slot at the rotor trailing edge would largely eliminate the tip clearance problem, but probably at the expense of the performance potential of the slot. Another location is forward of the rotor; here the objective would be the reduction of the rotor inlet boundary layer thickness.

The previously cited data from reference 6 and from the Low Speed Research Compressor are representative only of the time-average flows. Reference 5 presents hot-wire anemometer data which show the time-variation of the rotor discharge tip region flows. One of the more interesting features of these data is the discovery of a loss core, located approximately midway between adjacent blades, which grows in size with increased throttling. Apparently, therefore, only a portion of the tip region fluid

has low axial momentum. This observation suggests a bleed configuration designed to selectively bleed the low-axial-momentum fluid contained in the loss-core region while by-passing the high-axial-momentum fluid. Orientation of bleed holes in the tangential direction has a potential for accomplishing this. The high-axial-momentum fluid has a large axial velocity and therefore will not be aligned with the holes. The low-axial-momentum fluid has a low axial velocity and therefore will be aligned with the holes; this should tend to increase the effective-area coefficient of the holes and to take advantage of the large circumferential dynamic pressure that the low-axial-momentum fluid has.

The quantity of flow that must be removed in order to obtain a substantial gain in stall performance is not clear. However, the results of reference 6 show an axial-velocity-profile boundary layer displacement thickness of approximately 20% of the blade staggered spacing, (defined as the circumferential distance between blades times the cosine of the blade chord angle). Other unpublished data have shown approximately the same results with various aspect ratios and solidities. For the present geometry this displacement thickness is equivalent to approximately 3% of the compressor weight flow.

Selection and Design of Bleed and Blowing Configurations

Based on the foregoing considerations, three bleed and three blowing boundary-layer-control configurations were selected for experimental evaluation. Bleed configuration 1 is an annular flush slot in the casing located at the rotor leading edge (fig. 17). Bleed configurations 2 and 3 (fig. 18) consist of honeycomb sections in the casing, over the rotor, with the center lines of the cells tilted 55° and 70° from radial in the tangential direction. Each of the three bleed configurations was sized such that up to 4% of the compressor design weight flow can be extracted. Configurations 2 and 3 were designed such that the axial extent of the honeycomb sections can be increased as indicated in figure 18 to permit increased flow extraction, but these portions will be kept covered unless early test results indicate that more bleed area is required.

Blowing configuration 1 (fig. 19) consists of a series of discrete inclined holes in the casing slightly forward of the rotor blade. Blowing configurations 2 and 3 (fig. 20) are an annular flush slot located axially slightly forward of the rotor leading edge. Provisions for changing the direction of the flow from this slot were made and jet angles of approximately 35° and 20° from axial were tentatively selected as blowing configurations 2 and 3, respectively. Each of the three blowing configurations was sized such that up to 4% of the compressor design weight flow can be injected.

The following table summarizes the pertinent parameters used in the detailed designs.

Configuration Type	Bleed			Blowing		
Configuration Number	1	2	3	1	2	3
Effective-Area-Coefficient	.90	.75	.75	.92	.95	.95
Total Temperature, °R	520	650	650	642	642	642
Total Pressure, psia	14.70	17.95	17.95	22.75	22.75	22.75

The total pressure for the blowing configurations was calculated utilizing the choked flow pressure ratio and the tip casing static pressure at design. It was assumed that the blowing flow source in an actual engine application would be the rear stages of the (multistage) compressor. A line loss of 15% of the rear stage total pressure was assumed. An assumed adiabatic compression efficiency of 75% determined the blowing flow total temperature. A 40° swirl angle was assumed for purposes of sizing the slot.

The bleed configuration 1 total pressure and total temperature are standard inlet conditions. The effective-area coefficient for this configuration was selected to reflect the presence of the casing boundary layer. For bleed configurations 2 and 3, the absolute velocity in the tip region of the rotor was assumed entirely tangential with a magnitude equal to the average of the wheel speed and the design discharge tangential velocity. Euler's equation was applied to determine the tip region total temperature. The implied Mach number and the casing static pressure were used to determine the total pressure. The angle of the honeycomb, relative to a radial line, was selected as 55° for bleed configuration 2 and 70° for bleed configuration 3. These angles reflect the required radial velocity of the bleed flow.

APPENDIX

The continuity condition and the energy equation employed are, respectively, from reference 20,

$$W = \frac{2\pi g}{144}\int_{r_h}^{r_t} K_{bK}\,\rho\,V_z\,r\,d\,r \tag{A1}$$

and

$$(U\,V_\theta)_i - (U\,V_\theta)_{i-1} = g\,J\,c_p\,(T_i - T_{i-1}) \tag{A2}$$

where

$$T = t + \frac{V^2}{2\,g\,J\,c_p} \tag{A3}$$

The equation of state is

$$p = g\,\rho\,R\,t/144 \tag{A4}$$

with specific heats assumed constant.

The radial-equilibrium equation used for this design is from reference 11,

$$\frac{144}{\rho}\,\frac{\partial p}{\partial r} = \left[\frac{1 - M_z^2}{1 - M_m^2}\right]\left[\frac{V_\theta^2}{r} - \frac{D^2 r}{Dz^2}\,V_z^2\right] + \left[\frac{V_r}{1 - M_m^2}\right]\left[V_z\,\frac{\partial\,(r\,\mathrm{TAN}\epsilon)}{r\,\partial r}\right] \tag{A5}$$

This equation is exact (within the assumptions stated in reference 11) at stations external to the blade row. Since the one internal blade section that was employed was located approximately at the blade stacking axis, the other terms that normally appear in the radial-equilibrium equation for internal blade stations (see reference 11) were either zero or were judged to be negligible.

Because a form of the radial-equilibrium equation employing static pressure was used, an entropy gradient term does not appear explicitly. The entropy variations that result from radially non-constant losses are correctly accounted for, however, through the use of

$$\frac{T_i}{T_{i-1}} = \left(\frac{P_i}{P_{i-1}}\right)^{\frac{\gamma-1}{\gamma}} e^{\frac{S_i - S_{i-1}}{c_p}} \qquad \text{(A6)}$$

which results from the definition of entropy and the assumption of a perfect gas.

REFERENCES

1. Campbell, R. C.: Performance of Supersonic Ramp-Type Side Inlet with Combinations of Fuselage and Inlet Throat Boundary-Layer Removal, NACA RM E56A17, 1956.

2. Nichols, M. R., and Pierpont, P. K.: Preliminary Investigation of a Submerged Air Scoop Utilizing Boundary-Layer Suction to Obtain Increased Pressure Recovery, NACA TN 3437, 1955.

3. Erwin, John R., and Emery, James C.: Effect of Tunnel Configuration and Testing Technique on Cascade Performance, NACA Report 1016, 1951.

4. Pfenninger, W.: Recent Developments in the Field of Low Drag Boundary Layer Suction, The Laminar Flow Control Presentation for the Aeronautical Systems Division, Northrop Corporation Norair Division report NB 62-105, Revised September 1962, pp. 1-21.

5. Fessler, Theodore E., and Hartman, Melvin J.: Preliminary Survey of Compressor Rotor Blade Wakes and Other Flow Phenomena with a Hot Wire Anemometer, NACA RM E56A13, 1956.

6. Mager, Artur, Mahoney, John J., and Budinger, Ray E.: Discussion of Boundary Layer Characteristics Near the Wall of an Axial Flow Compressor, NACA Report 1085, 1952.

7. Herzig, Howard Z., Hansen, Arthur G., and Costello, George R.: A Visualization Study of Secondary Flows in Cascades, NACA Report 1163, 1954. (Supersedes NACA TN 2947).

8. Dean, Robert C., Jr.: The Influence of Tip Clearance on Boundary Layer Flow in Rectilinear Cascade, Report #27-3, Gas Turbine Lab., M.I.T., 1954.

9. Kussoy, Marvin I., and Bachkin, Daniel: Comparison of Performance of Two Aerodynamically Similar 14-inch Diameter Single Stage Compressor Rotors of Different Chord Length, NACA RM E57I03, 1958.

10. Swan, W. C.: An Experiment with Aspect Ratio as a Means of Extending the Useful Range of a Transonic Inlet Stage of an Axial Flow Compressor, Journal of Engineering for Power, Trans. ASME, Series A, Vol. 86, July 1964, pp. 243-246.

11. Smith, L. H., Jr.: The Radial Equilibrium Equation of Turbomachinery, Journal of Engineering for Power, Trans. ASME, Series A, Vol. 88, 1966, pp. 1-12.

12. Robbins, William H., Jackson, Robert J., and Lieblein, Seymour: Blade-Element Flow in Annular Cascades, Aerodynamic Design of Axial-Flow Compressors, NASA SP-36, Chapt. VII, 1965, pp. 227-254.

13. Miller, Genevieve R., Lewis, George W., Jr., and Hartman, Melvin J.: Shock Losses on Transonic Compressor Blade Rows, Journal of Engineering for Power, Trans. ASME, Series A, Vol. 83, July 1961, Page 235.

14. Smith, Leroy H., Jr., and Yeh, Hsuan: Sweep and Dihedral Effects in Axial-Flow Turbomachinery, Journal of Basic Engineering, Trans. ASME, Series D, Vol. 85, 1963, pp. 401-416.

15. Carter, A. D. S.: The Low Speed Performance of Related Aerofoils in Cascade; National Gas Turbine Establishment, Report Number R55, September 1949, Aeronautical Research Council, C.P. No. 29, (12883).

16. Robbins, William H., and Glaser, Fredrick: Experimental Investigation of the Effect of Circumferential Inlet Flow Distortion on the Performance of a Five-Stage Axial-Flow Research Compressor with Transonic Rotors in all Stages, NACA RM E57J17, 1957.

17. Cornell, W. G.: ASME Paper No. 57-F-19, ASME Transactions, Vol. 80, #4, Page 791-799.

18. Cox, P. B.: Phase I Summary Technical Report of the Calendar Year 1962, Air Force Marquardt Contributing Engineering Program, Volume II of VIII, Jet Compressor Research, Section VI, Marquardt Corporation Report 25,065, 22 February 1963.

19. Vogel, Dipl. Ing. R.: Theoretical and Experimental Investigation of Ejectors, "Maschineubautechnik", 5, Jg., Heft 12/1956.

20. Gianati, Charles C., Jr., and Finger, Harold B.: Design Velocity Distribution in Meridional Plane, Aerodynamic design of Axial-Flow Compressors, NASA SP-36, Chapt. VIII, 1965, pp. 255-278.

Table 1 - Aeromechanical data for rotor blade

Stresses (psi)		
Average root centrifugal stress		24,372
Total stress at root		
	Convex side	33,307
	Trailing edge	33,447
	Concave side	23,820
Total stress at shroud		
	Convex side	621
	Trailing edge	16,916
	Concave side	14,520
Maximum estimated stall vibratory stress at shroud		
	Convex side	14,200 (32% endurance)
Blade natural frequencies at design speed (cps)		
1st flexural	472	
2nd flexural	1493	
3rd flexural	1994	
1st torsional	1207	
Tip Untwist at design speed (deg)		1.3
Material		6Al-4V-Ti Titanium alloy

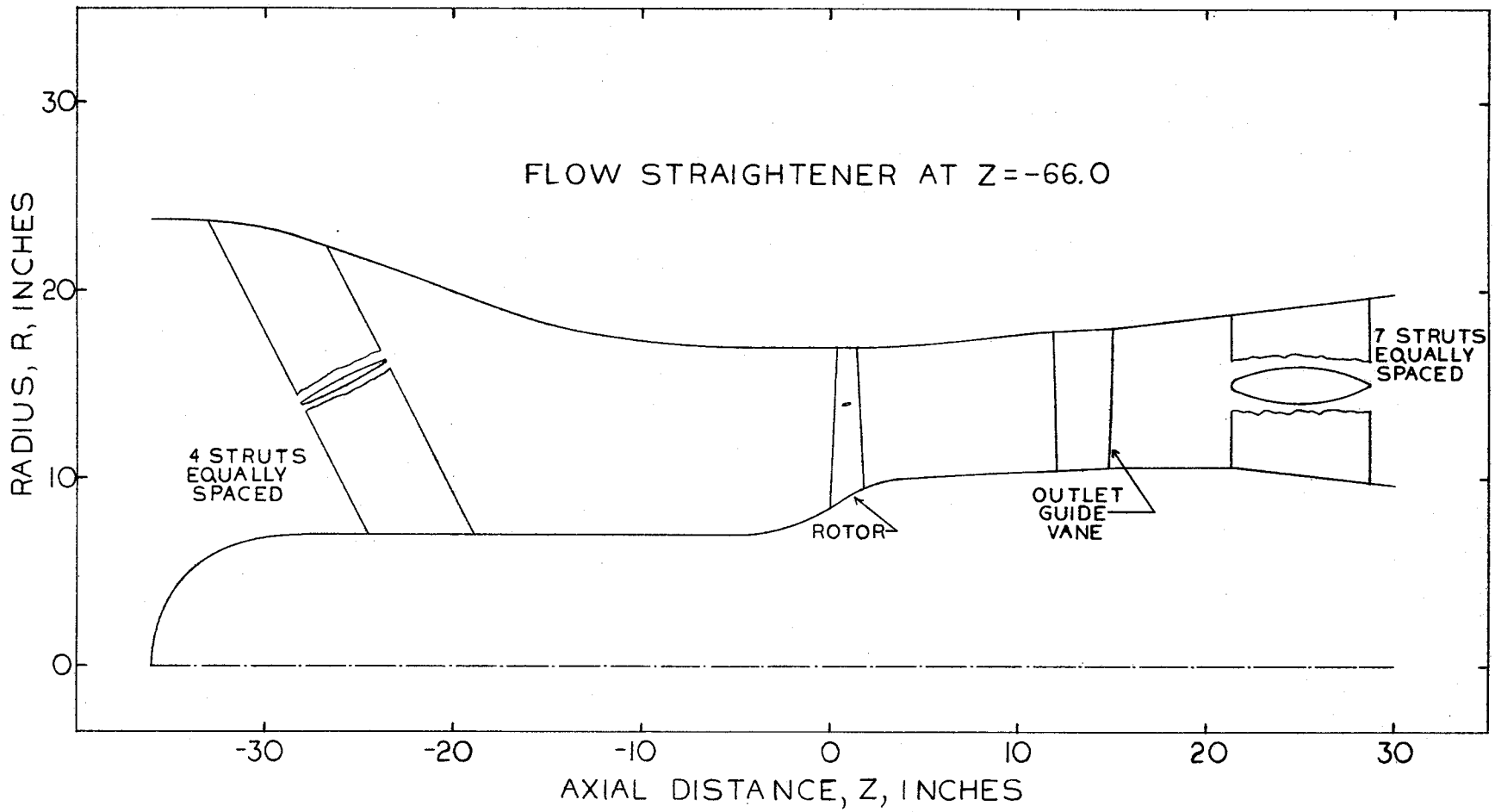

FIGURE 1. COMPRESSOR FLOWPATH

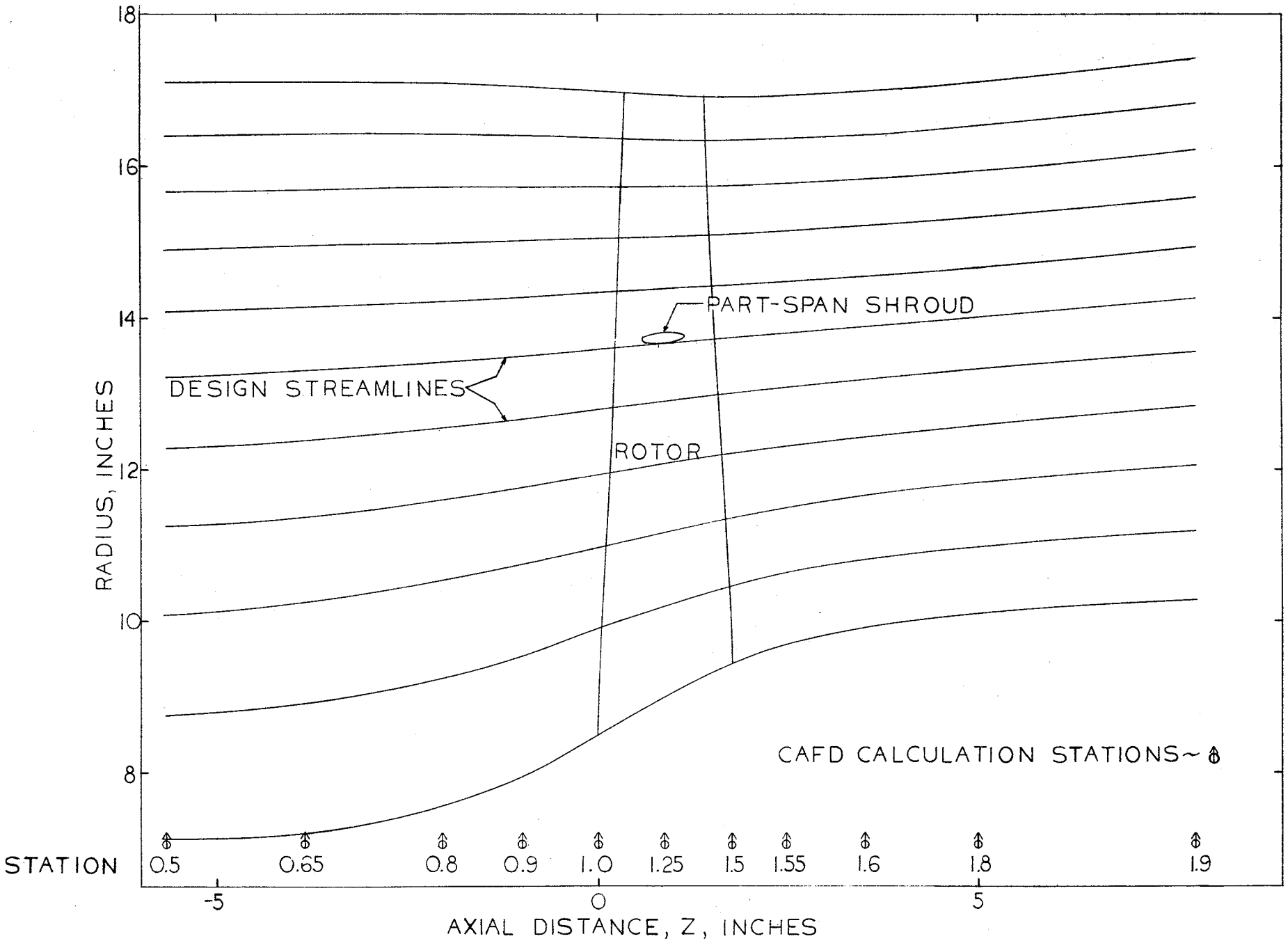

FIGURE 2. DESIGN ROTOR FLOW FIELD

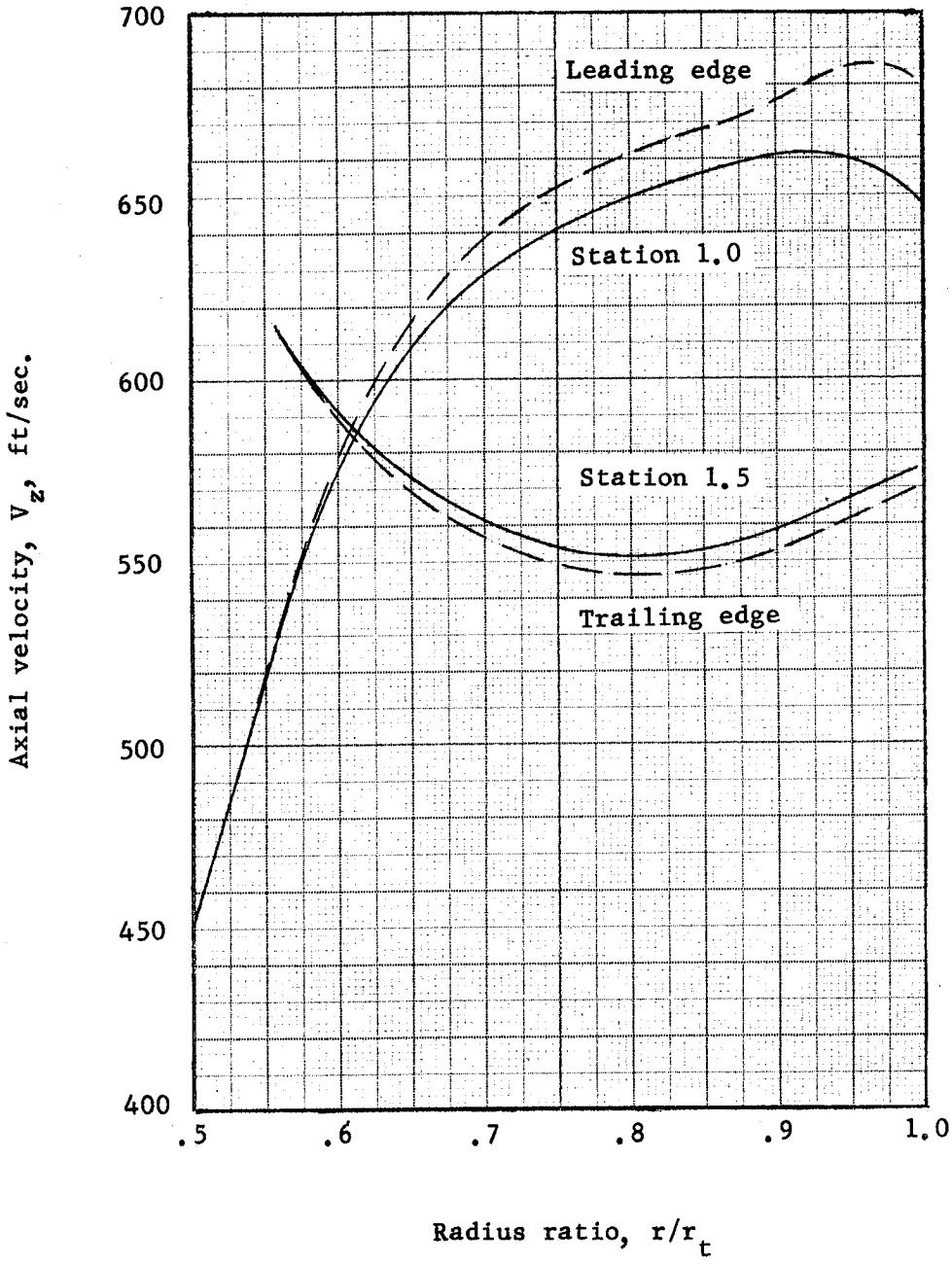

Figure 3. - Radial variation of design axial velocity.

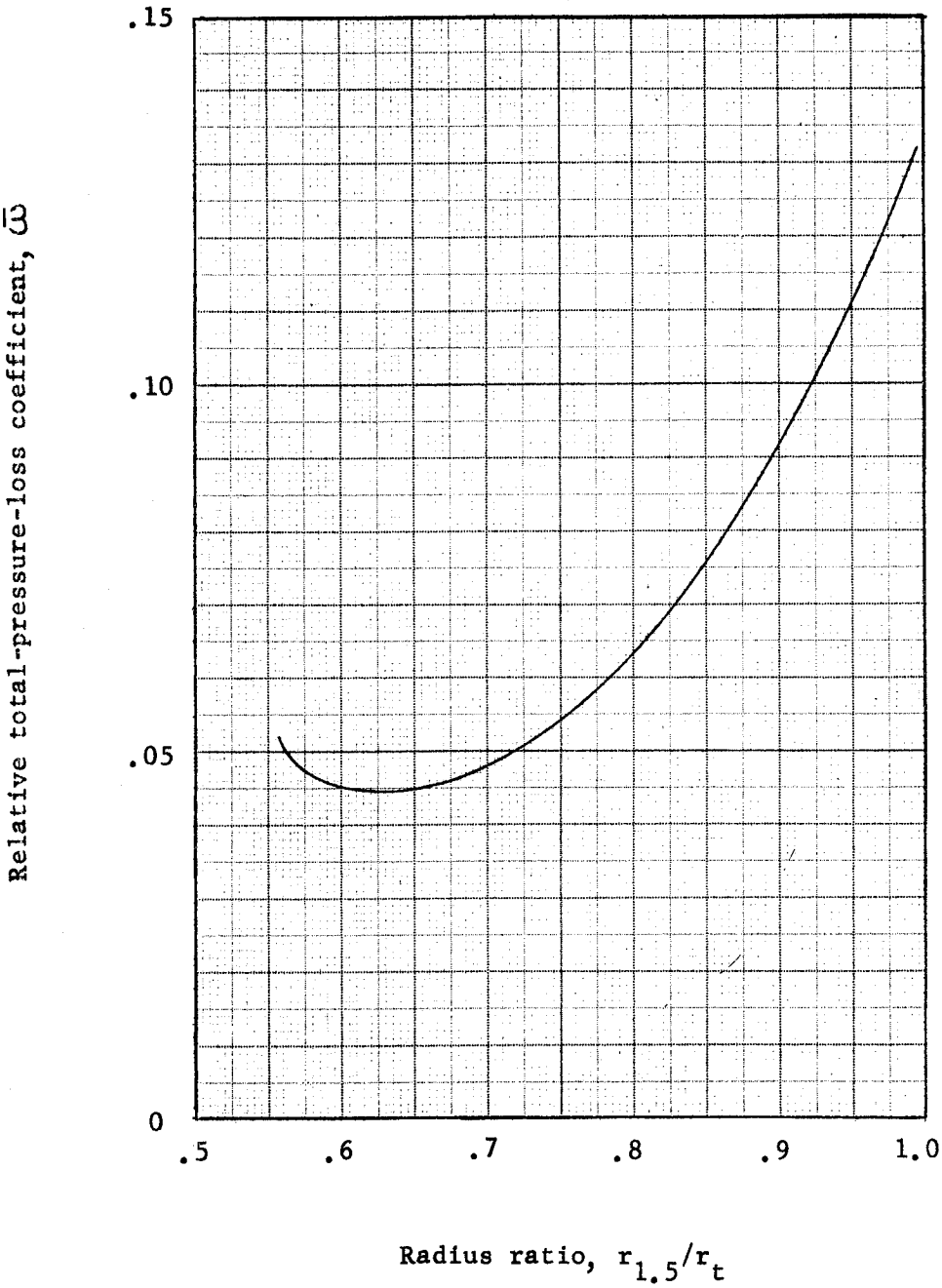

Figure 4. - Radial variation of design relative total-pressure-loss coefficient.

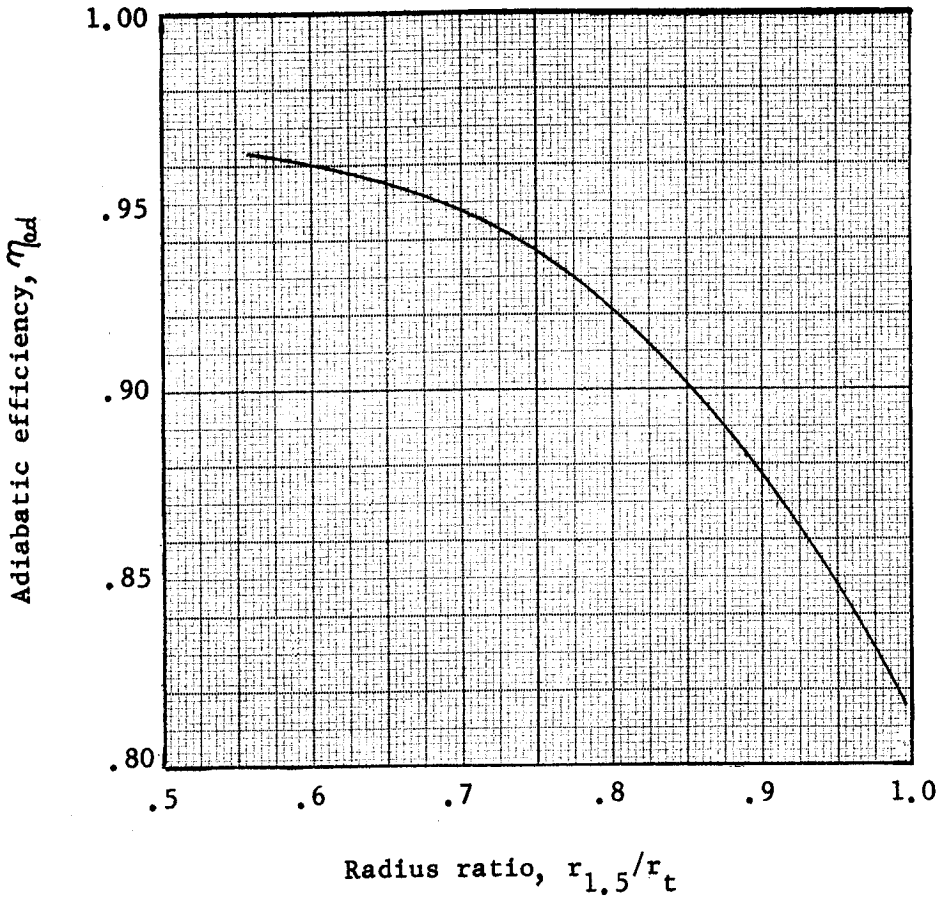

Figure 5. - Radial variation of design adiabatic efficiency.

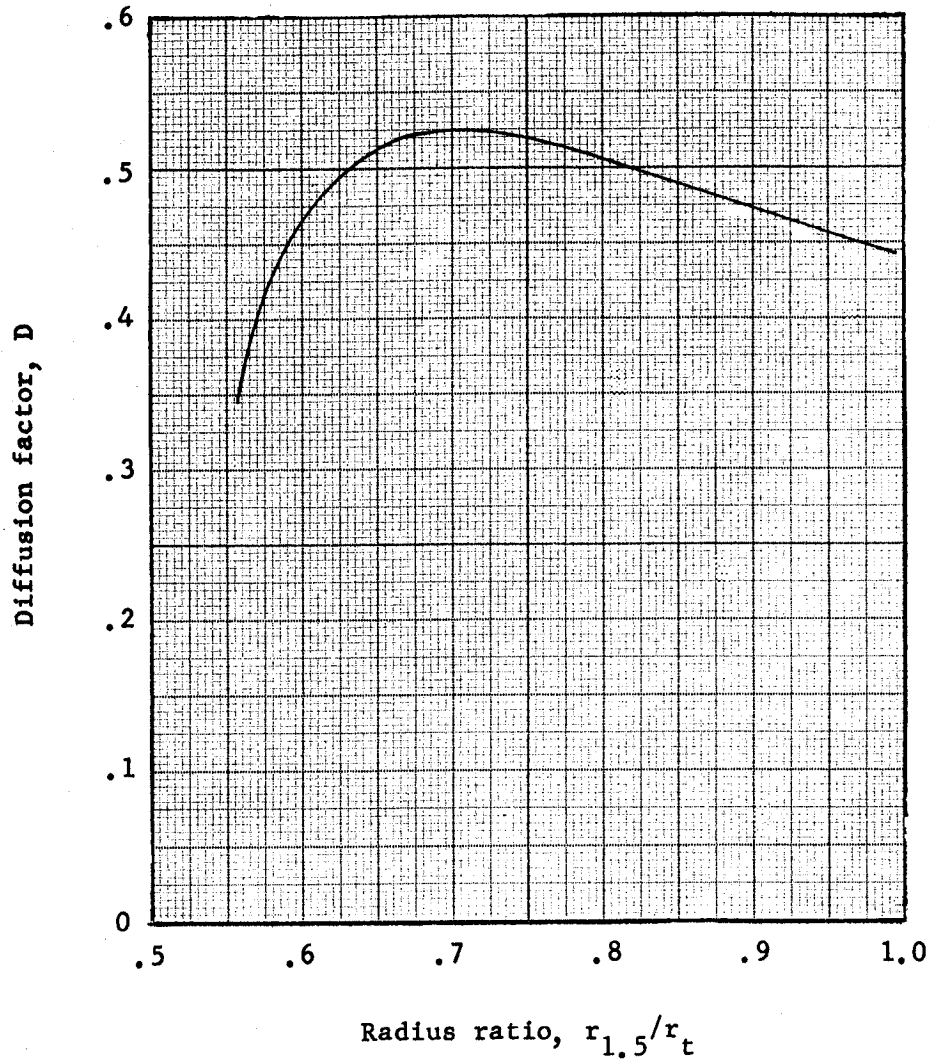

Figure 6. - Radial variation of design diffusion factor.

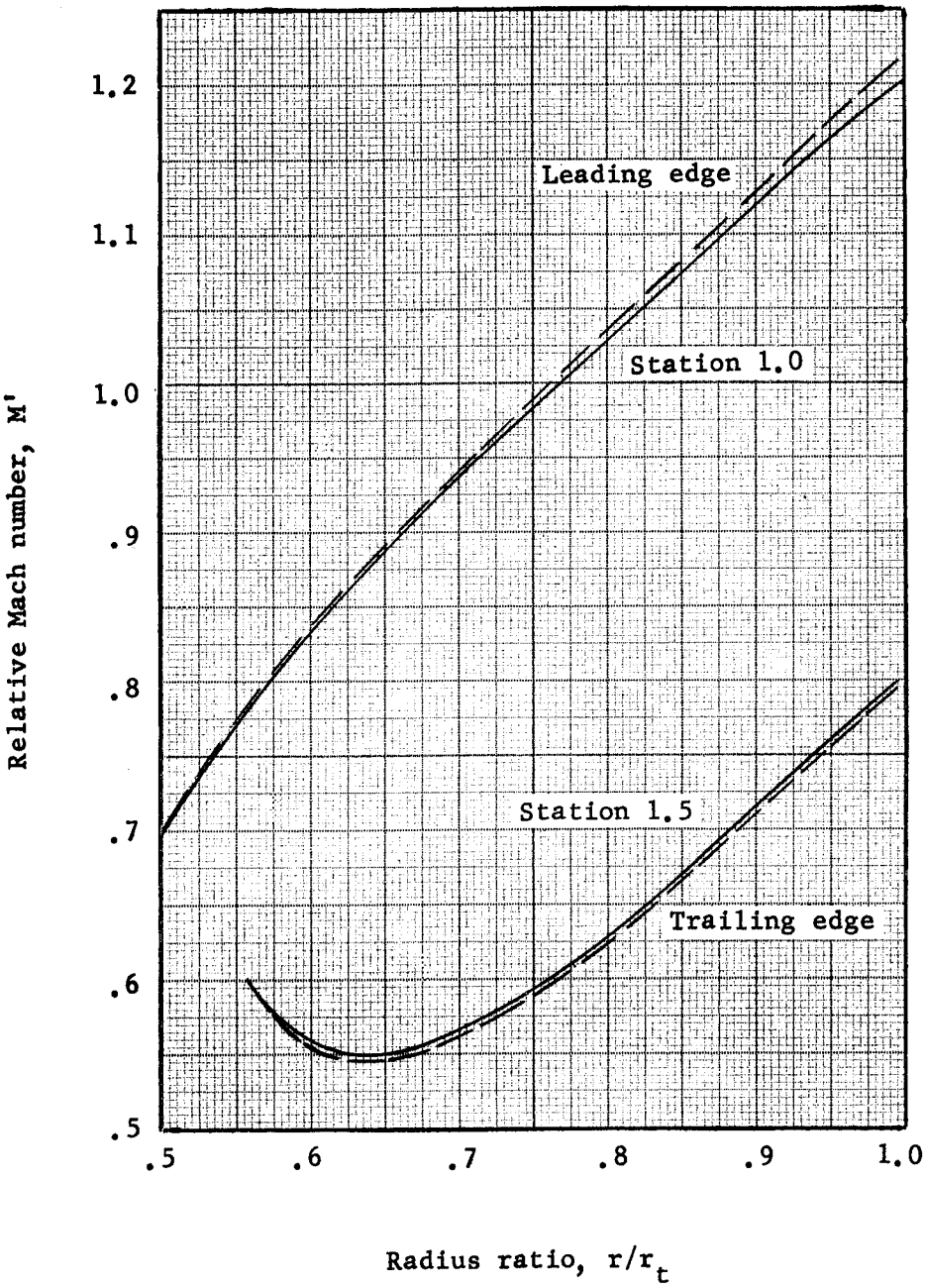

Figure 7. - Radial variation of design relative Mach number.

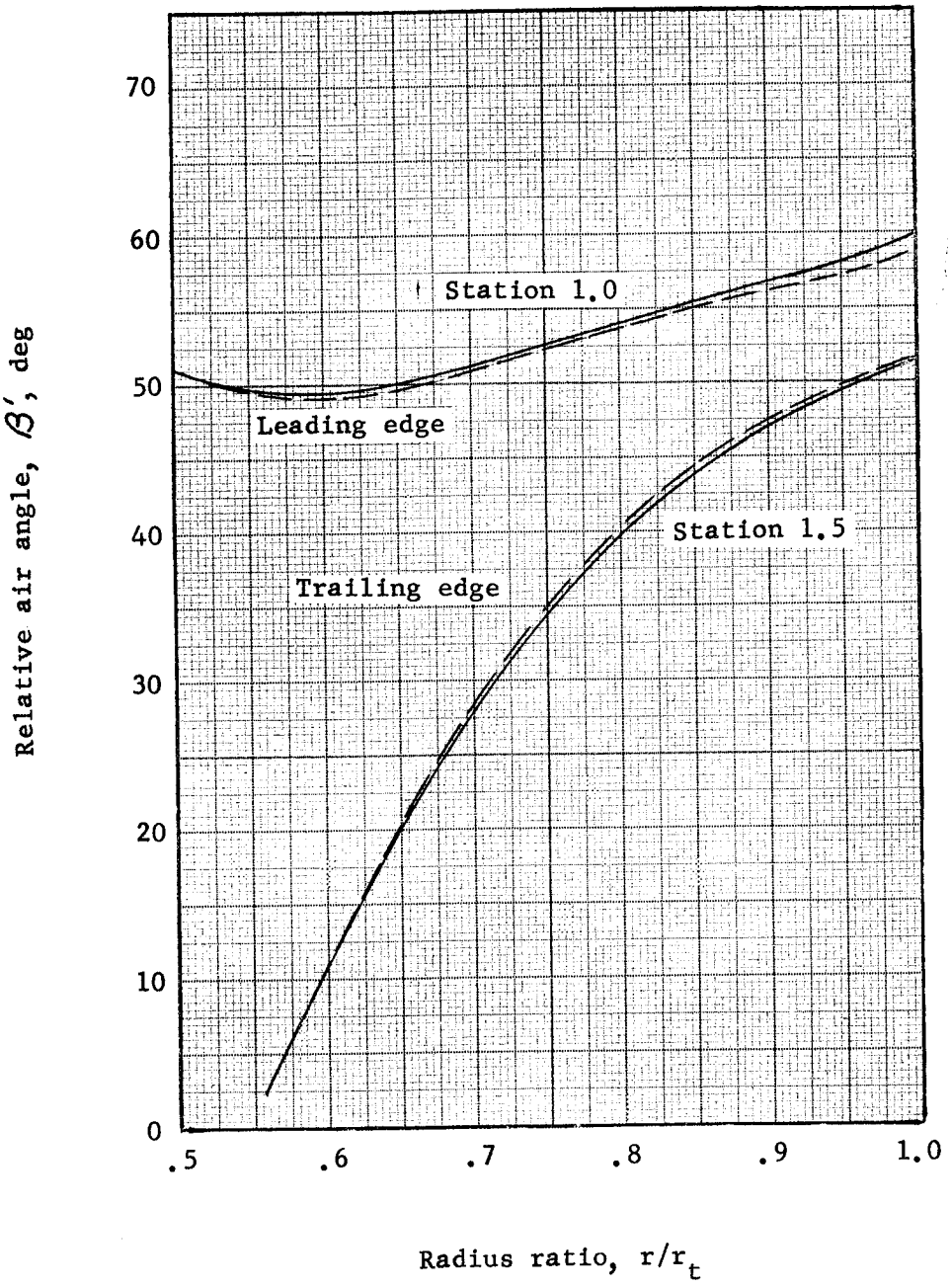

Figure 8. - Radial variation of design relative air angle.

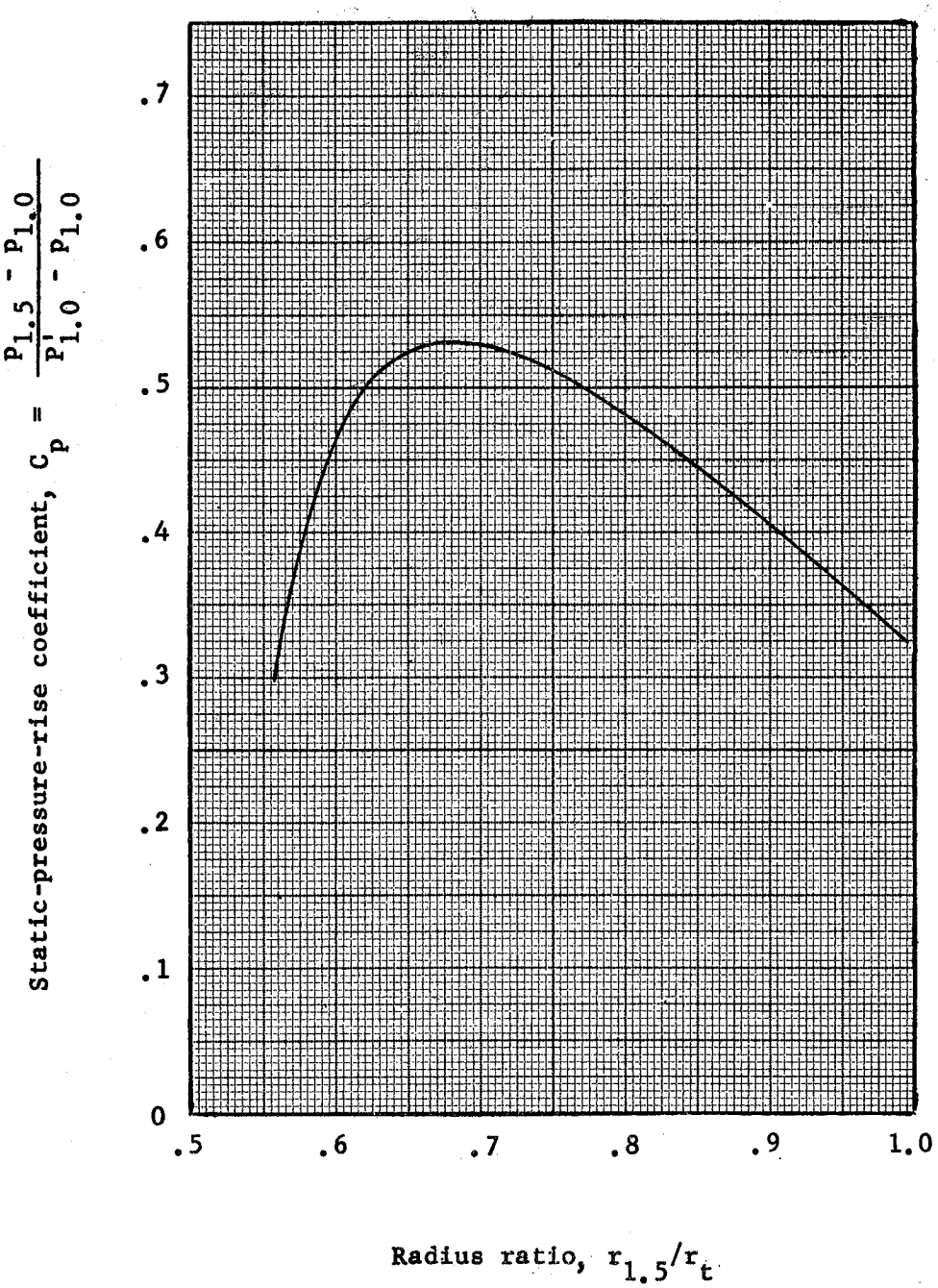

Figure 9. - Radial variation of static-pressure-rise coefficient.

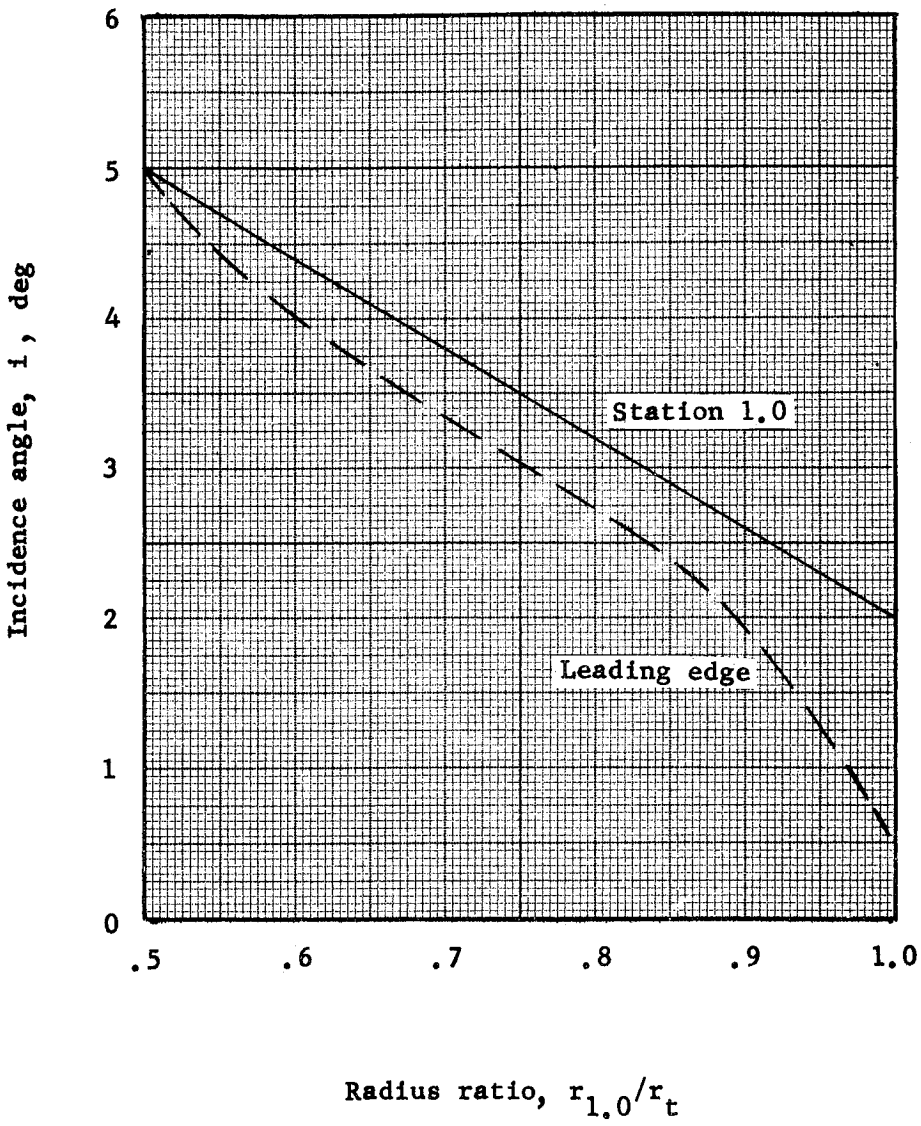

Figure 10. - Radial variation of design incidence angle.

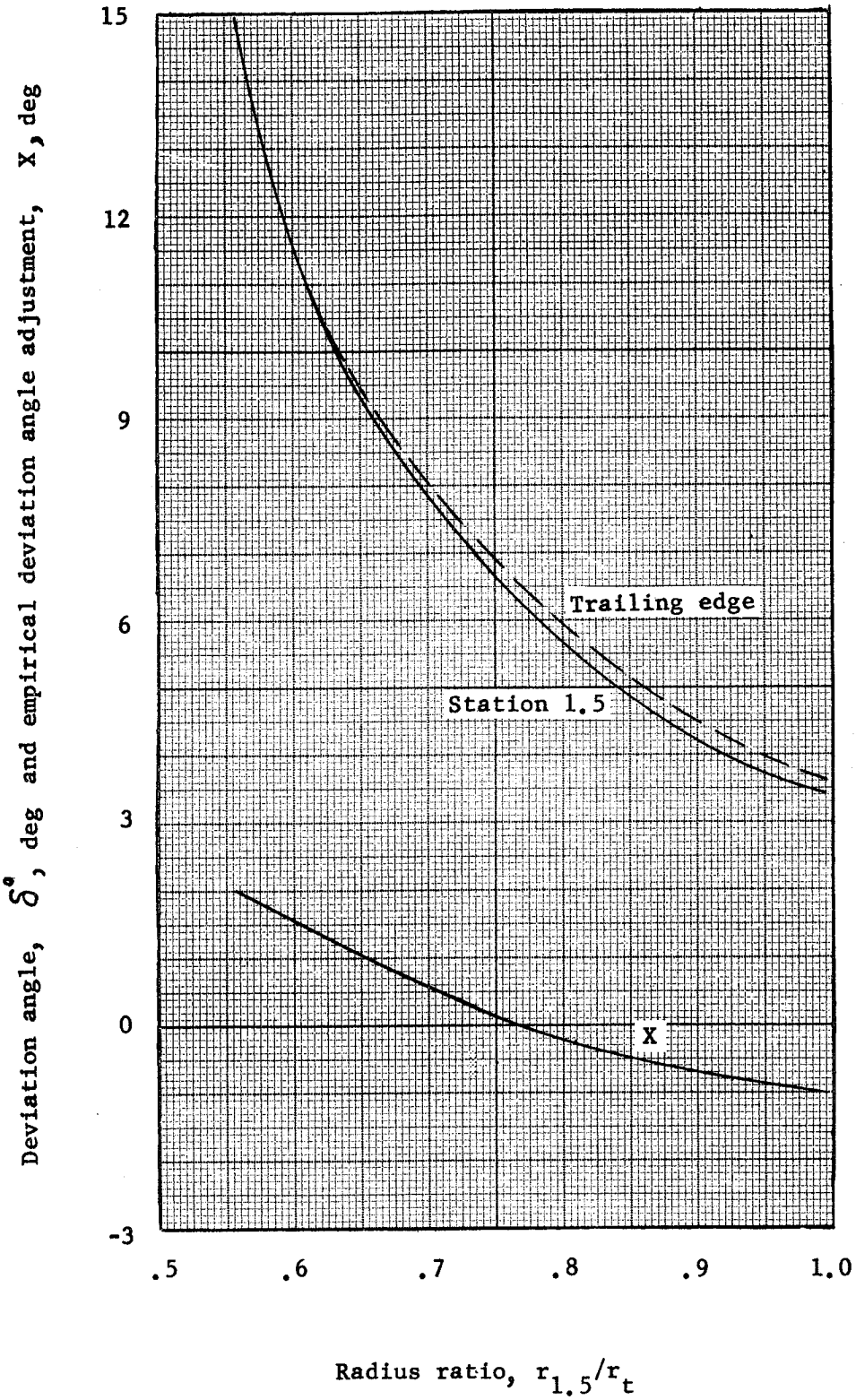

Figure 11. - Radial variation of design deviation angle and empirical deviation angle adjustment.

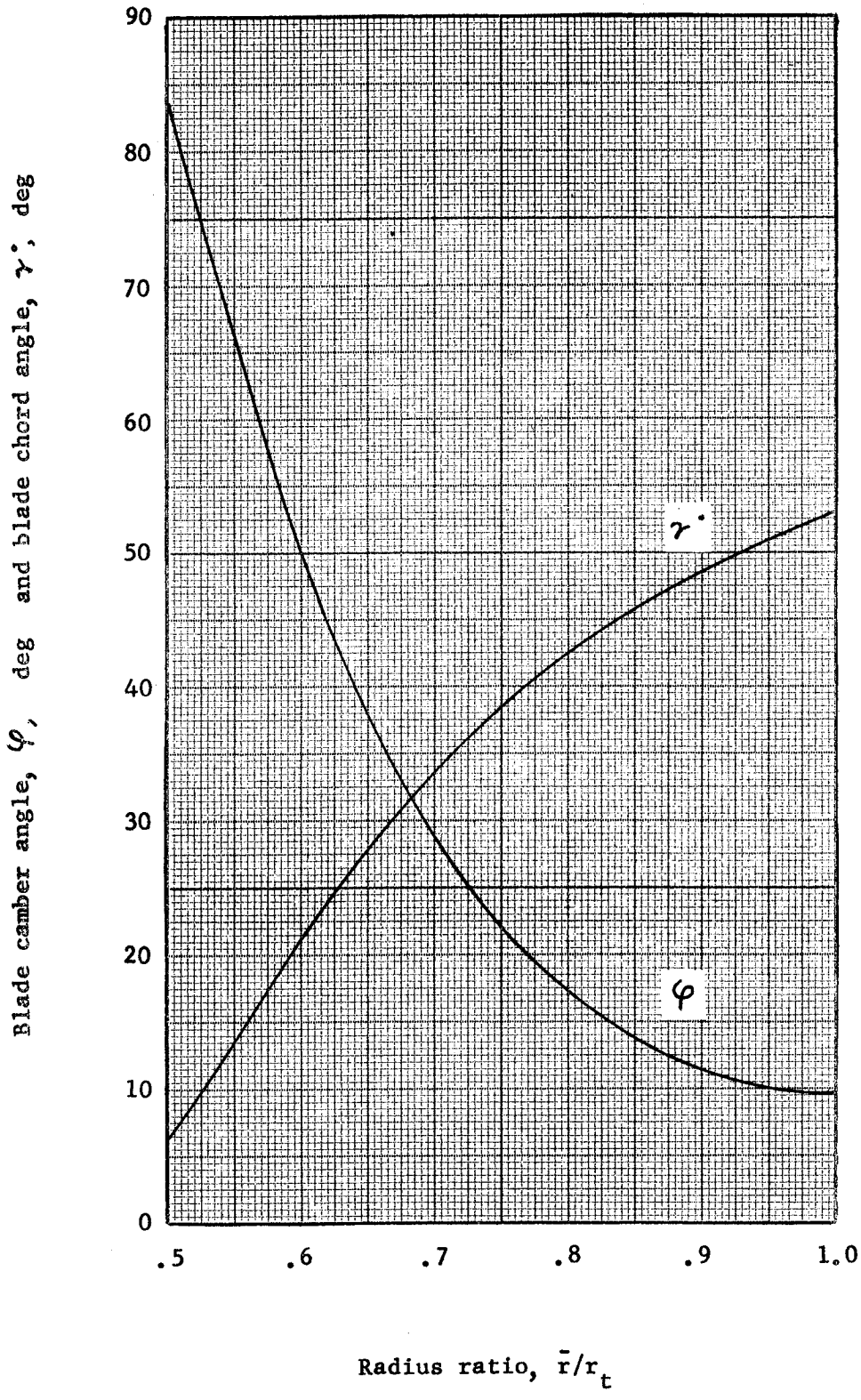

Figure 12. - Radial variation of cylindrical - section blade camber angle and blade chord angle.

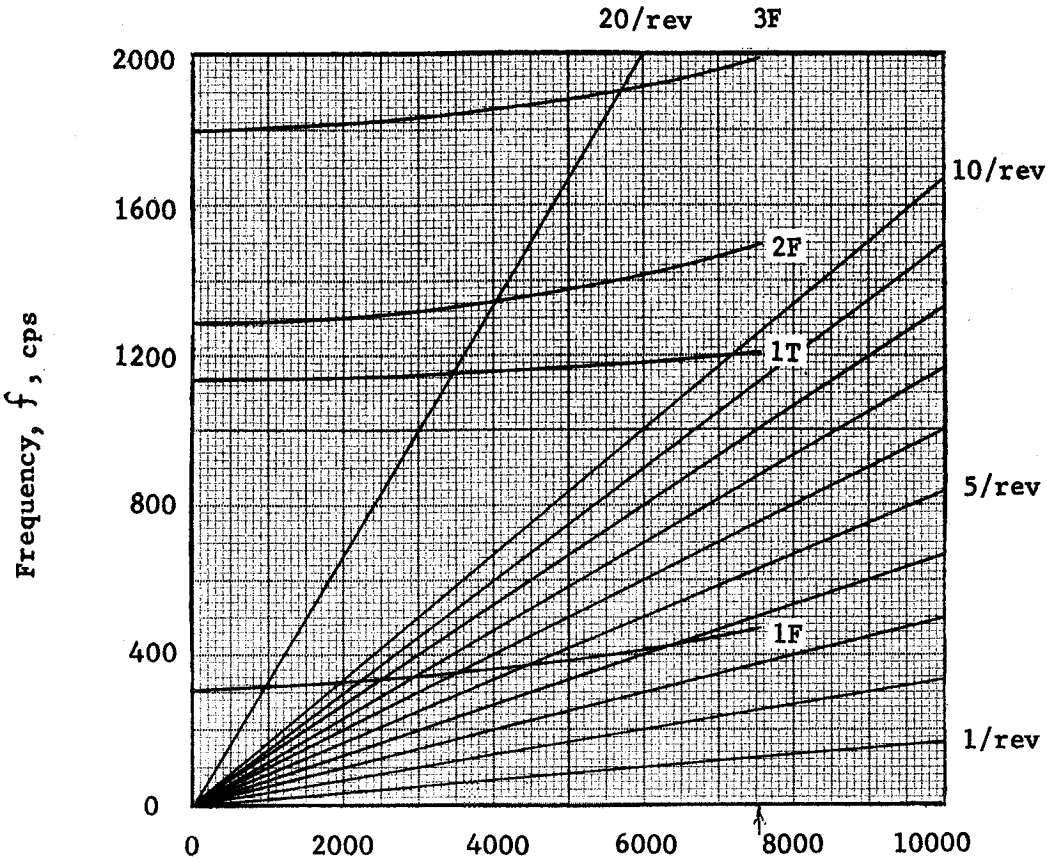

1F = 1st. flexural frequency
1T = 1st. torsional frequency
2F = 2nd. flexural frequency
3F = 3rd. flexural frequency
↑ = Design speed 7550 rpm

Figure 13. - Rotor blade Campbell diagram.

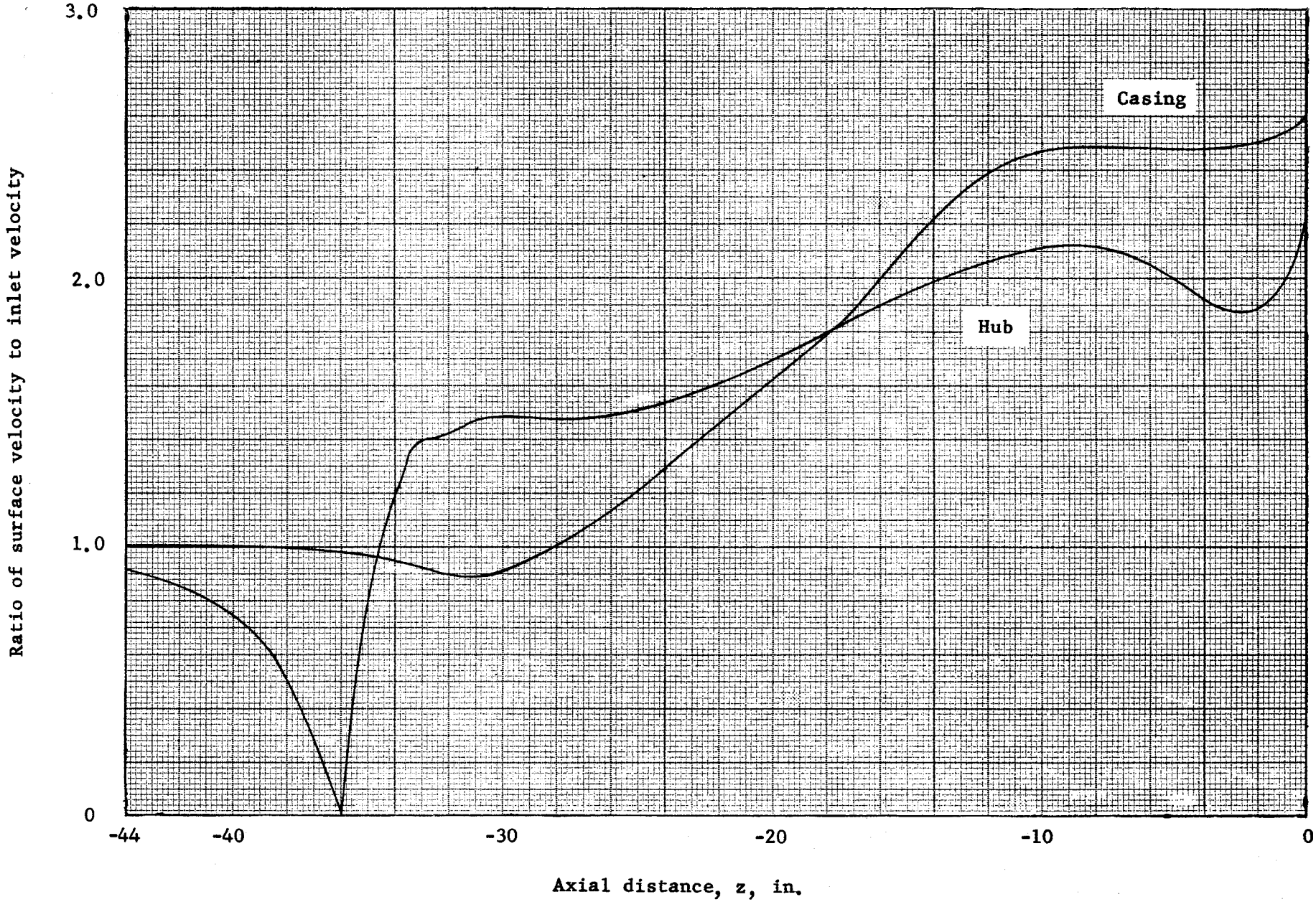

Figure 14. - Surface velocity distribution through inlet contraction region. (Incompressible axisymmetric solution)

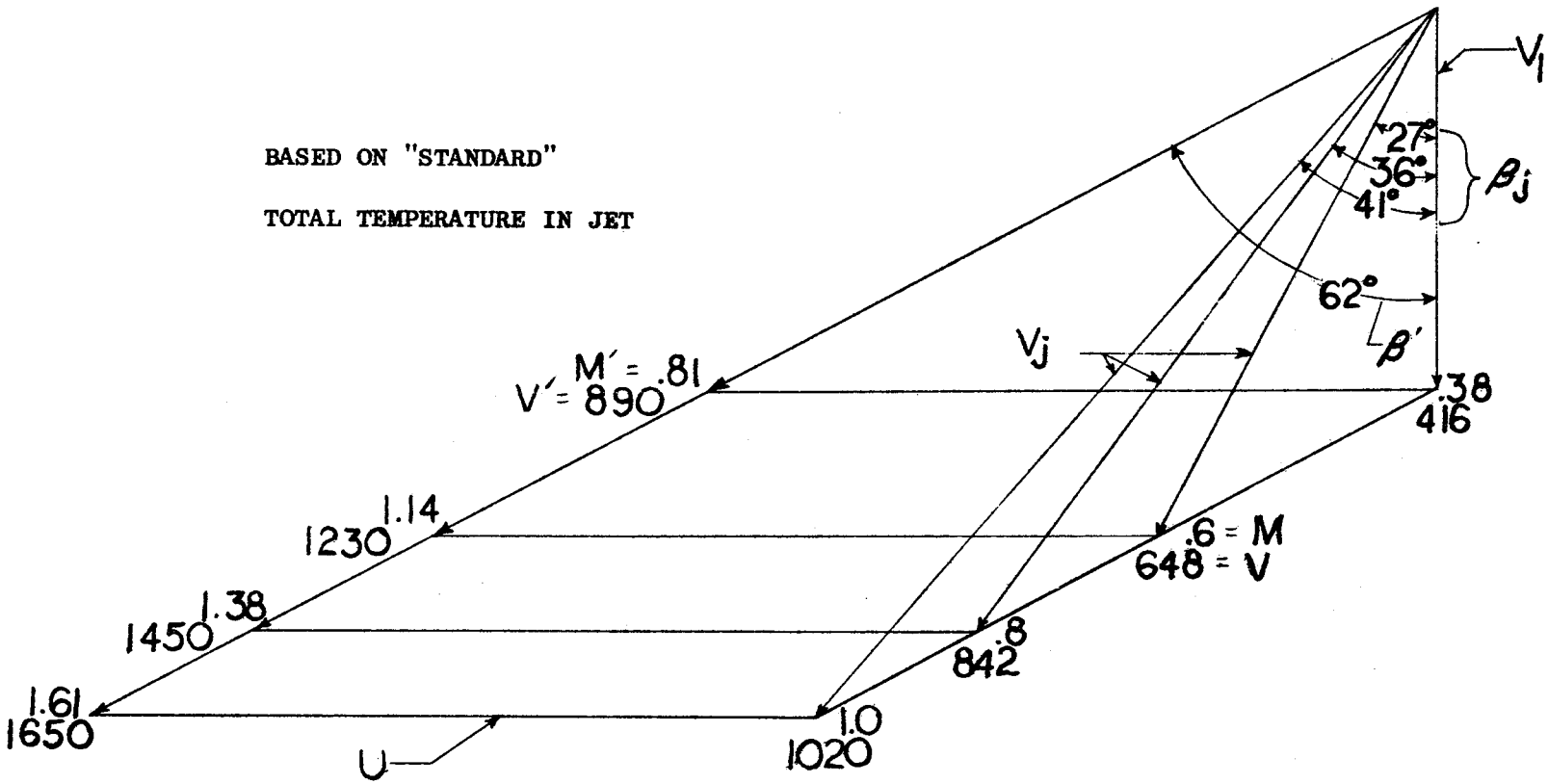

Figure 15. - VARIATION OF JET ANGLE WITH JET VELOCITY FOR CONSTANT ROTOR INCIDENCE AT 70% SPEED.

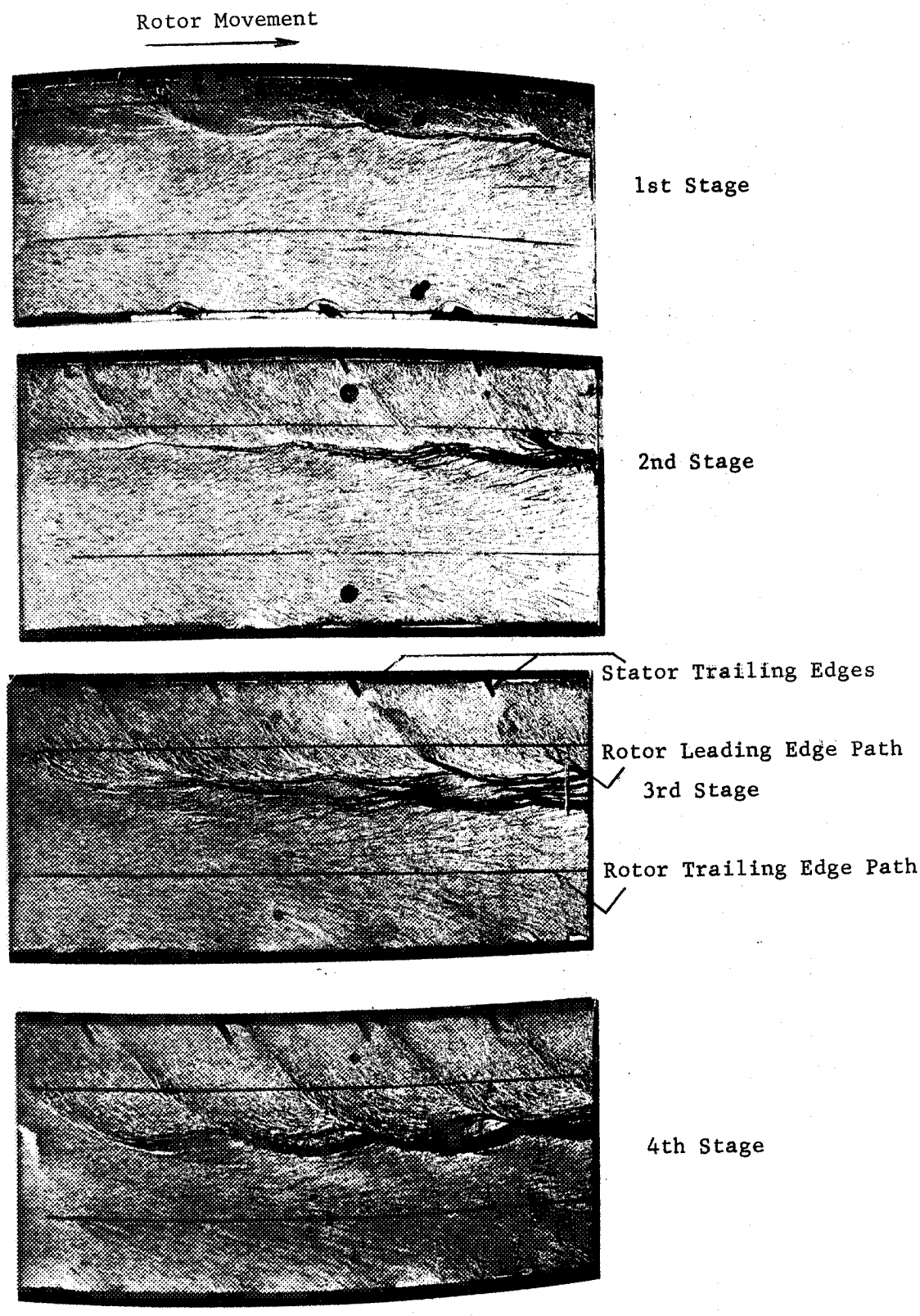

Figure 16. - Lamp black and oil traces of flow over rotor tips.

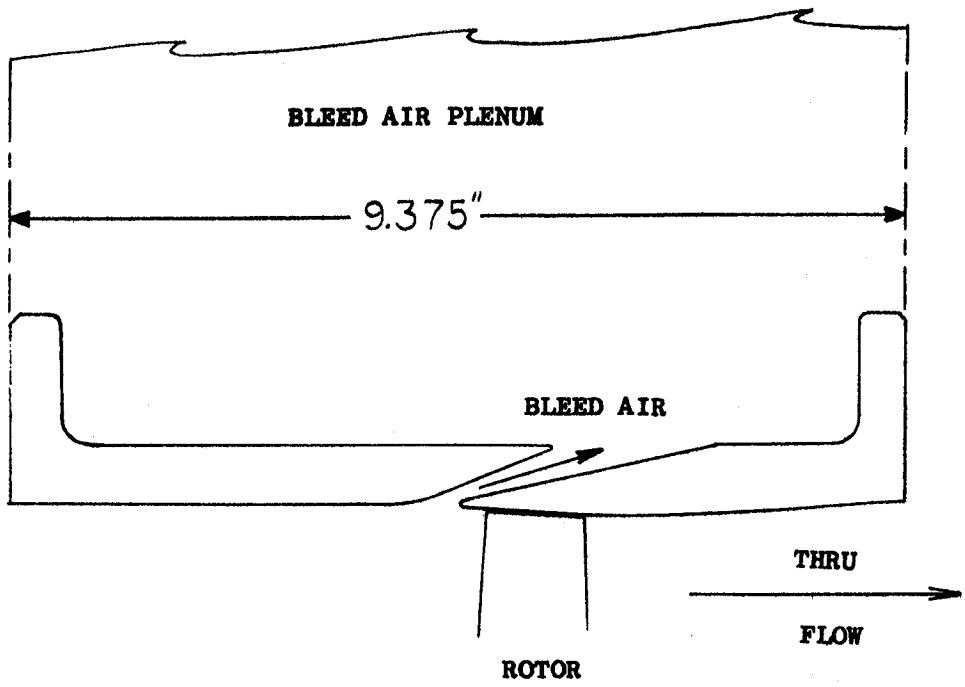

Figure 17. - BLEED CONFIGURATION 1.

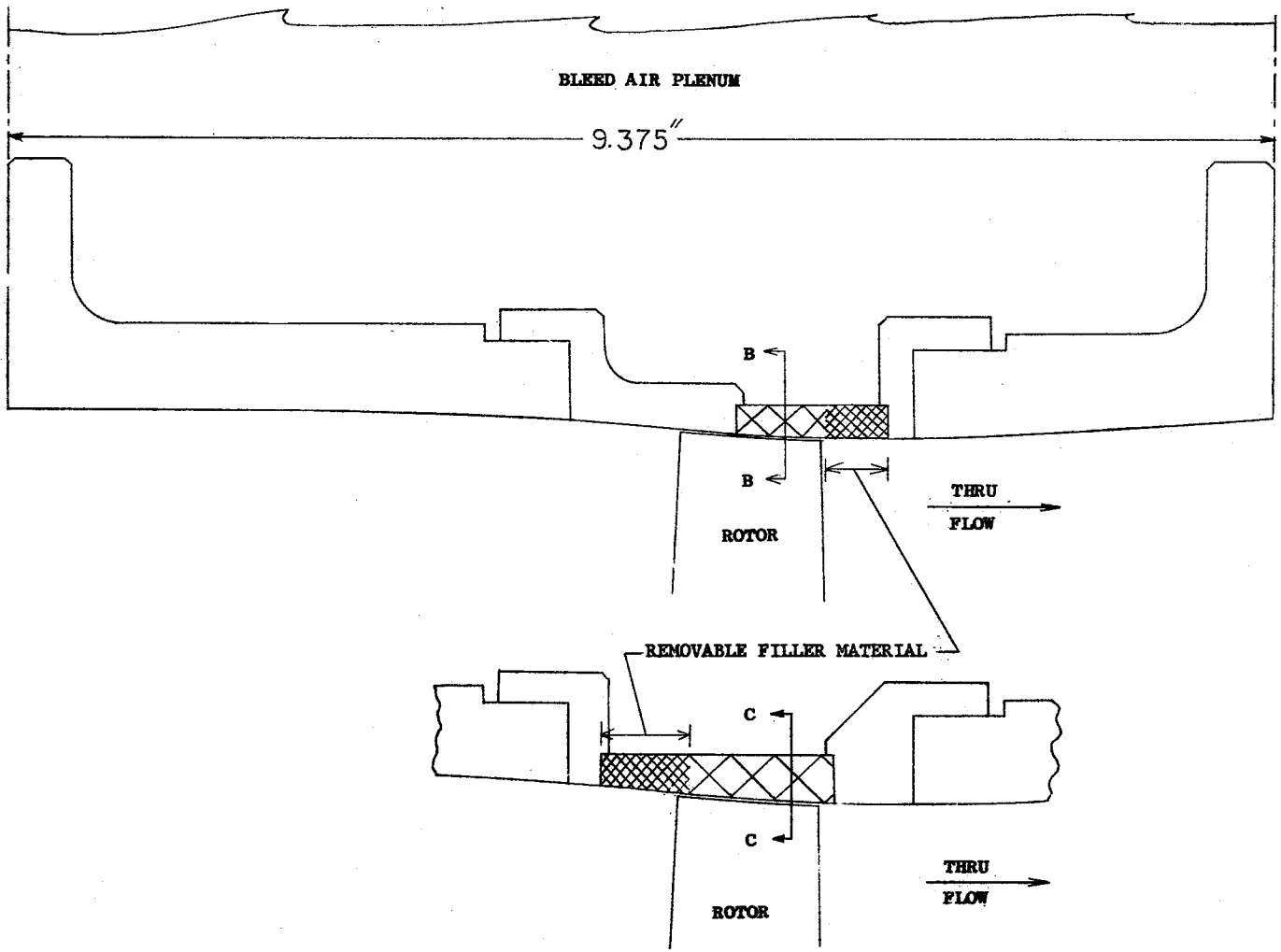

A. MERIDIONAL VIEWS

Figure 18. - BLEED CONFIGURATIONS 2 (TOP) and 3 (BOTTOM).

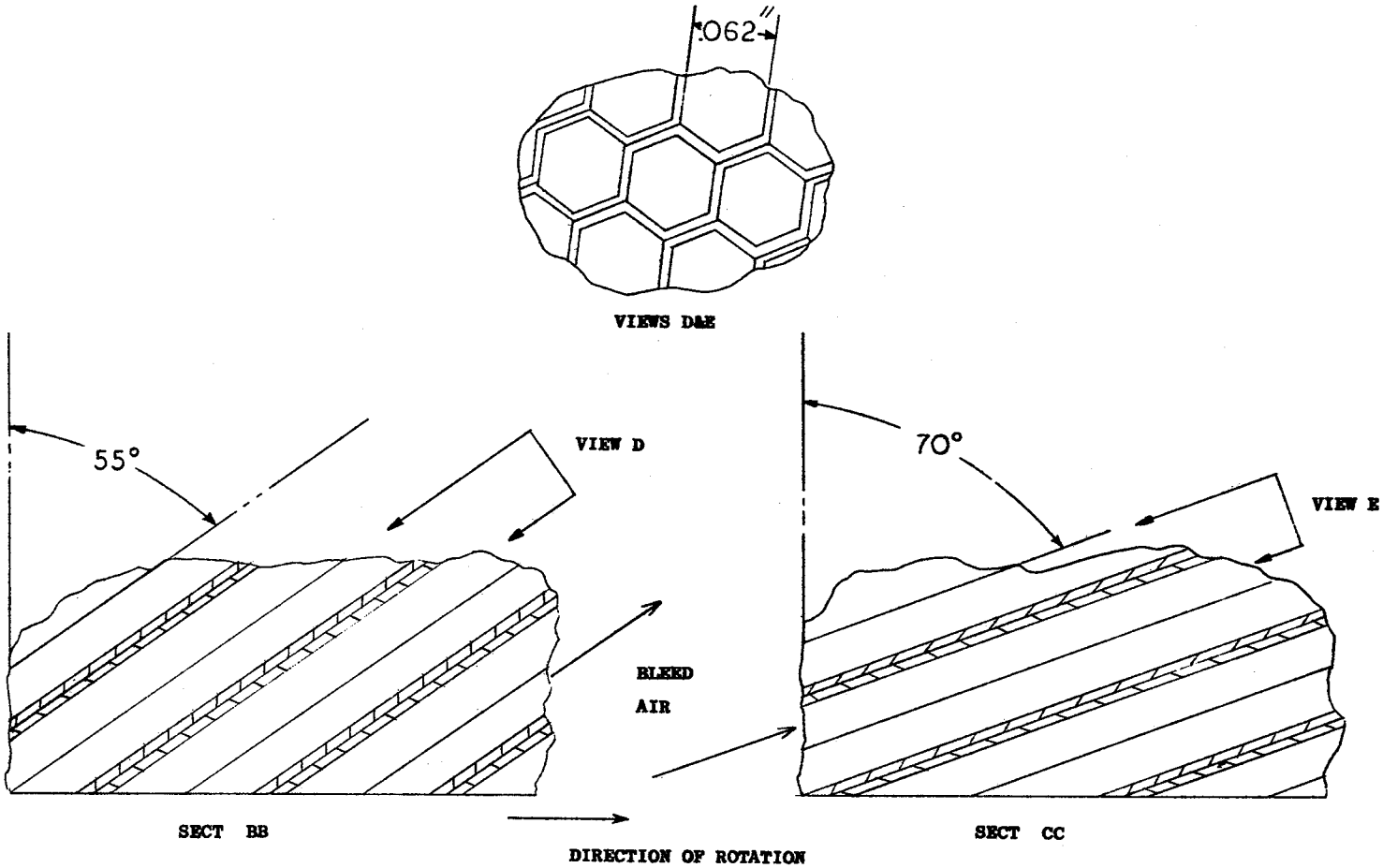

B. HONEYCOMB DETAILS

Figure 18. - CONCLUDED

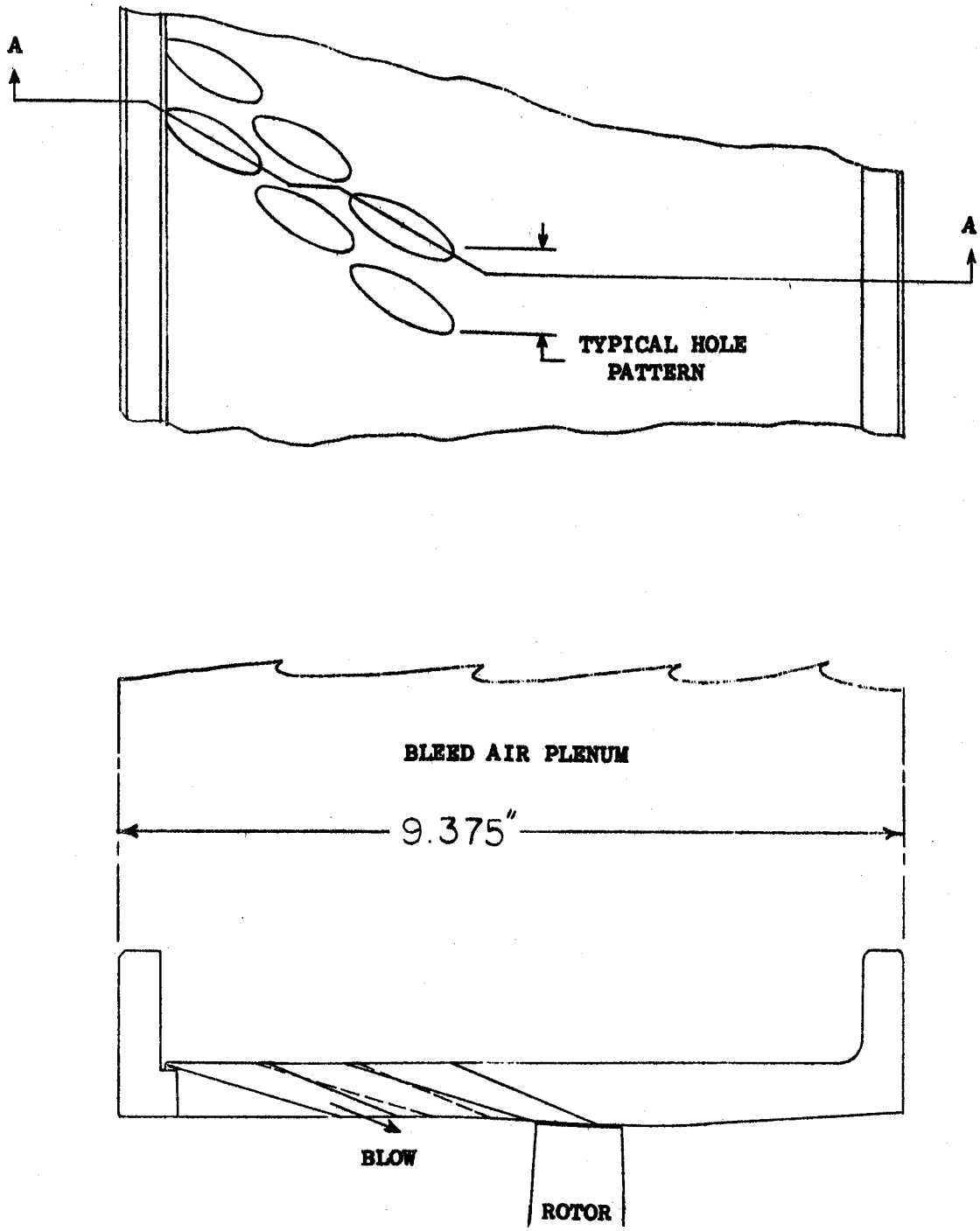

Figure 19. - BLOWING CONFIGURATION 1.

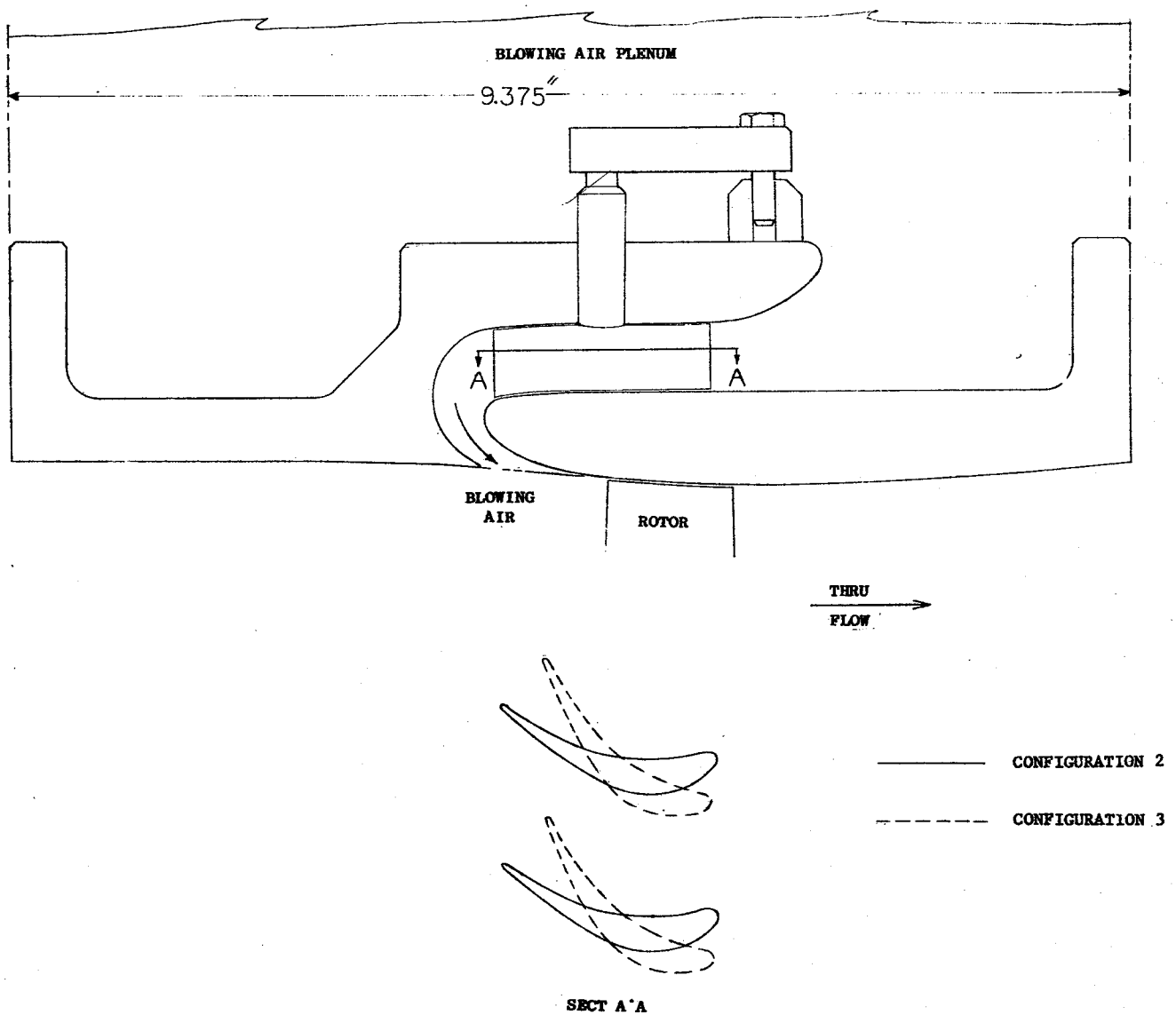

Figure 20. - BLOWING CONFIGURATIONS 2 AND 3.

REPORTS DISTRIBUTION LIST FOR

CONTRACT NAS3-7618

PRELIMINARY ANALYSIS AND DESIGN REPORT

1. NASA-Lewis Research Center
21000 Brookpark Road
Cleveland, Ohio 44135

Attention: Report Control Office MS 5-5	1
Technical Utilization Office MS 3-19	1
Library	1
Fluid System Component Division MS 5-3	1
Pump & Compressor Branch MS 5-9	6
I. I. Pinkel MS 5-3	1
A. Ginsburg MS 5-3	1
Thomas B. Shillito MS 5-3	1
M. J. Hartmann MS 5-9	1
W. A. Benser MS 5-9	1
D. M. Sandercock MS 5-9	1
L. J. Herrig MS 5-9	1
C. L. Ball MS 5-9	1
J. Howard Childs MS 60-4	1
Dr. W. H. Roudebush MS 60-6	1
John DeFord MS 60-5	1
W. Beede MS 60-6	1
J. McAulay MS 60-6	1
SST Branch MS 60-6	22

2. NASA Scientific & Technical Information Facility
P. O. Box 5700
Bethesda, Maryland
Attention: NASA Representative — 6

3. FAA Headquarters
800 Independence Avenue, SW
Washington, D.C. 20553
Attention: Gordon M. Bain — 1
Jack O. Charshafian SS/120 — 1

4. NASA Headquarters
Washington, D.C. 20546
Attention: N. F. Rekos (RAP) — 1

5. U.S. Army Aviation Material Laboratory
Fort Eustis, Virginia
Attention: John White — 1

6. Headquarters
Wright Patterson AFB, Ohio 45433
Attention: J. L. Wilkins, SESOS — 1
S. Kobelak, APTP — 1
R. P. Carmichael, SESSP — 1

7. Department of the Navy
Bureau of Weapons
Washington 25, D.C.
Attention: Robert Brown, RAPP14 — 1

8. Department of the Navy
Bureau of Ships
Washington, D.C. 20360
Attention: G. L. Graves — 1

9. NASA-Langley Research Center
Technical Library
Hamption, Virginia 23365
Attention: Mark R. Nichols — 1
John V. Becker — 1

10. Pratt & Whitney Aircraft
Florida Research & Development Center
P. O. Box 2691
West Palm Beach, Florida 33402
Attention: R. A. Schmidtke — 1
C. L. Joslin — 1
W. R. Alley — 1
B. N. Torrel — 1
B. A. Jones — 1
B. S. Saven — 1

11. Pratt & Whitney Aircraft
400 Main Street
East Hartford, Connecticutt
Attention: J. A. Fligg 1
A. W. Stubner 1
W. D. Harshbarger 1
P. Tramm 1
M. J. Keenan 1
B. B. Smyth 1

12. Allison Division, GMC
Dept. 8894, Plant 8
P. O. Box 894
Indianapolis, Indiana 46206
Attention: J. N. Barney 1
R. H. Carmody 1
G. E. Holbrook 1
B. A. Hopkins 1
M. L. Miller 1
Library 1

13. Northern Research & Engineering
219 Vassar Street
Cambridge 39, Massachusetts
Attention: R. A. Novak 1
K. Ginwala 1

14. General Electric Company
Flight Propulsion Division
Cincinnati, Ohio 45215
Attention: J. W. Blanton J-19 1
W. G. Cornell K-49 1
J. R. Erwin J-162 1
E. E. Hood/J. C. Pirtle J-165 1
J. F. Klapproth H-42 1
J. W. McBride H-44 1
L. H. Smith H-50 1
S. N. Suciu H-32 1
J. B. Taylor J-168 1
Technical Information Center N-32 1

15. General Electric Company
1000 Western Avenue
West Lynn, Massachusetts
Attention: D. P. Edkins Bldg. 2-40 1
F. F. Ehrich Bldg. 2-40 1
L. H. King Bldg. 2-40 1
R. E. Neitzel Bldg. 2-40 1
Dr. C. W. Smith Library Bldg. 2-40M 1

16. Curtiss-Wright Corporation
Wright Aeronautical
Woodridge, New Jersey
Attention: S. Lombardo 1
B. Provenzale 1
J. Wiggins 1

17. Air Research Manufacturing Company
402 South 36th Street
Phoenix, Arizona 85034
Attention: Robert O. Bullock 1
John H. Daman 1

18. Air Research Manufacturing Company
8951 Sepulveda Boulevard
Los Angeles, California 90009
Attention: Dr. N. Van Le 1

19. Avco Corporation
Lycoming Division
550 South Main Street
Stratford, Connecticut
Attention: Clause W. Bolton 1

20. Continental Aviation & Engineering Corporation
12700 Kercheval
Detroit, Michigan 48215
Attention: Eli H. Benstein 1
Howard C. Walch 1

21. Solar
San Diego, California 92112
Attention: P. A. Pitt 1
Mrs. L. Walper 1

22. Goodyear Atomic Corporation
Box 628
Piketon, Ohio
Attention: C. O. Langebrake 2

23. Union Carbide Corporation 1
Nuclear Division
Oak Ridge Gaseous Diffusion Plant
P. O. Box "P"
Oak Ridge, Tennessee 37830
Attention: Mr. R.G. Jordan

24. The Boeing Company
Commercial Airplane Division
P. O. Box 3991
Seattle, Washington 98124
Attention: G. J. Schott, M.S. 80-66 1